NONUNIFORM SHEAR STRAINS IN TORSIONAL KOLSKY BAR TESTS
ON SOFT SPECIMENS

Adam Sokolow and Mike Scheidler

msp

msp

# NONUNIFORM SHEAR STRAINS IN TORSIONAL KOLSKY BAR TESTS ON SOFT SPECIMENS

ADAM SOKOLOW AND MIKE SCHEIDLER

We investigate inertial effects in torsional Kolsky bar tests on nearly incompressible, soft materials. The results are relevant for materials with instantaneous elastic shear modulus on the order of 1–1000 kPa and density on the order of water. Examples include brain tissue and many other soft tissues and tissue surrogates. We have conducted one- and three-dimensional analyses and simulations to understand the stress and strain states that exist in these materials in a torsional Kolsky bar test. We demonstrate that the short loading pulses typically used for high strain-rate (e.g., 700/s) tests do not allow the softer specimens to "ring-up" to uniform stress and strain states and that consequently the shear stress versus shear strain data reported in the literature are erroneous. We also show that normal stress components, which are present even in quasistatic torsion of nonlinear elastic materials, can be amplified in dynamic torsion tests on soft materials.

## 1. Introduction

Kolsky bar tests are widely used to study strain-rate effects in inelastic solids [Gray 2000; Chen and Song 2011]. In a *compression* Kolsky bar test, a relatively thin specimen is sandwiched between two bars. Impact at one end of the incident bar generates a compressive wave that travels along the bar, through the specimen, and into a transmission bar. The goal of this test is to subject the specimen to uniform uniaxial stress and uniform (biaxial) strain at a prescribed axial strain-rate. These uniform conditions can often be achieved after an initial "ring-up" period involving multiple wave reflections from the specimen-transmission bar and specimen-incident bar interfaces. Once uniform conditions have been achieved in the specimen, the axial stress, axial strain, and axial strain-rate histories in the specimen can be deduced from strain gage measurements on the elastic bars: the axial stress is proportional to the strain in the transmission bar, and the axial strain-rate is proportional to the strain in the incident bar generated by the wave reflected from the specimen and transmission bar. A similar approach utilizes a *torsional* wave in the Kolsky bar instead of a compressive wave [Gilat 2000; Hartley et al. 1985]. Typically, a number of test are performed at different strain-rates, and the data are presented as a family of stress-strain curves with each curve corresponding to a different (approximately constant) strain-rate.

The standard Kolsky bar techniques work well on metals, composites, and stiff polymers and have provided useful data for the calibration of viscoplastic constitutive models and rate-dependent failure models. More recently, Kolsky bar tests have been performed on gelatins and soft biological specimens with the goal of providing data for the calibration of viscoelastic constitutive models for these materials. However, considerable difficulties have been encountered with these softer specimens. Radial accelerations in compression tests may result in stress states that are not uniaxial, that is, radial and
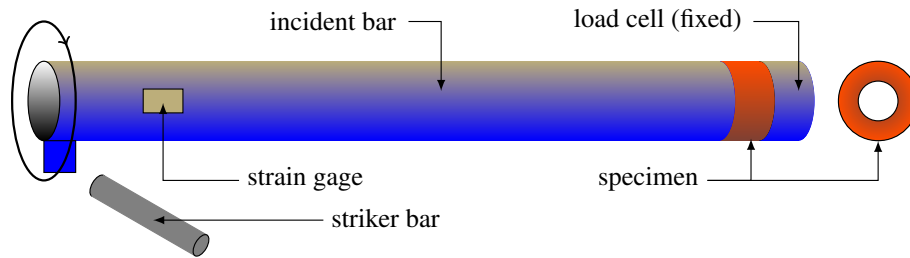
**Figure 1.** Schematic (not to scale) of the experimental setup for the modified torsional Kolsky bar described in [Nie et al. 2013]. Only the specimen is included in the simulations.

hoop stresses that are a significant fraction of the axial stress but cannot be measured [Scheidler and Kraft 2010; Scheidler et al. 2011; Warren and Forrestal 2010]. Studies utilizing compression Kolsky bar techniques purportedly removed radial inertia effects by switching from disk-shaped specimens to annular specimens [Chen and Song 2011]. It was later shown that annular specimens are also plagued by radial inertia effects and that the observed increases in axial stress at high strain-rates were falsely attributed to viscoelastic properties of the specimen [Scheidler and Kraft 2010; Sanborn 2011; Sanborn et al. 2012].

Recently, a variation of the torsional Kolsky bar test has been developed for studying the strain-rate sensitivity of very soft materials and applied to bovine brain tissue [Nie et al. 2013; Sanborn et al. 2012]. In this modified torsion test, the transmission bar is replaced with a torque load cell in order to generate a stronger signal than could be obtained from strain gage measurements on a transmission bar; see Figure 1. The faces of thin annular specimens are glued to the incident bar and the load cell. Strain gage measurements in the incident bar are used to infer the rate of the angle of twist at the specimen-incident bar interface and consequently a volumetric average of the shear strain-rate in the specimen. Integration yields the angle of twist at the interface and consequently a volumetric average of the shear strain in the specimen. The radially averaged shear stress at the specimen-load cell interface is deduced from the torque measured at the load cell. The stress-strain curves in [Nie et al. 2013] are obtained by plotting this *radially averaged shear stress at the load cell* versus the *volume averaged shear strain in the specimen.* Comparison of stress-strain curves at different strain-rates could (in principle) yield information on the rate-sensitivity of the shear stress. Nie et al. [2013] performed Kolsky bar tests on bovine brain tissue at an average shear strain-rate of 700/s. Analogous quasistatic tests at strain-rates of 0.01/s and 1/s were performed for comparison, and the results appeared to indicate a substantial increase in shear stress in the dynamic test.

The effects of radial inertia in this torsional Kolsky bar test are expected to be much lower than in a compression test at the same strain-rate. *However, for specimens as soft as brain tissue, the effects of axial inertia (i.e., torsional wave propagation) may be significant.* The shear wave speeds in the softer specimens are so low that even for thin (i.e., 1–2 mm thick) specimens there may be insufficient time for the specimen to "ring-up" to an axially uniform state of stress, strain, and strain-rate. In particular, if the shear strain has large axial variations, then the shear strain at the specimen-load cell interface may not be close to the average shear strain used to generate the stress-strain curves in [Nie et al. 2013], in which case their "stress-strain curves" would not provide valid constitutive data. Likewise, the shear strain-rate at the specimen-load cell interface may not be close to the reported average shear strain-rate.

Torsion and compression tests on soft materials differ in another significant way. As noted above, for compression tests, the desired uniaxial stress state may be impossible to achieve dynamically, but uniaxial

stress can always be achieved quasistatically if frictional effects at the specimen faces are negligible. However, even in a quasistatic torsion test, the desired state of *pure shear stress* is impossible to achieve except for infinitesimal deformations. Significant normal stresses can develop in finite deformation quasistatic torsion. While radial stresses can be reduced by the use of annular specimens, axial and hoop stresses may not be negligible. Furthermore, the glued boundary conditions for annular specimens can be expected to result in axial variations in the stress and strain state even in a quasistatic test since radial deformations are prohibited at the ends of the specimen but not in the interior. Thus, unlike quasistatic compression tests, the stress state in quasistatic torsion tests on soft materials is already quite complicated, and inertial effects in the corresponding dynamic test will further complicate these stress states. Even if the full stress state could be measured in a dynamic torsion test, it would be difficult to sort out the role of inertial effects from nonlinear elastic or viscoelastic effects without results for the corresponding quasistatic case for comparison. This problem is compounded by the fact that in the torsional Kolsky bar test only the torsional ($\theta z$) stress component can be inferred from the test data, and this is known only on the face of the specimen in contact with the load cell.

In view of these issues, we have undertaken numerical simulations of both dynamic and quasistatic torsion tests on soft and nearly incompressible materials. To simplify the dynamic simulations, the incident bar and the load cell are not included; they are replaced with appropriate boundary conditions at the specimen ends. Unlike a real torsion test, the simulations provide the complete stress and strain states at each point in the specimen although a constitutive model must necessarily be assumed. A linear elastic constitutive model was used in our one-dimensional simulations, and a nonlinear elastic constitutive model was used in most of our three-dimensional simulations.

Of course, soft tissues are viscoelastic (and poroelastic as well), and the goal of Kolsky bar tests on these inelastic materials is to quantify their strain-rate sensitivity. However, performing numerical simulations with elastic constitutive models is a particularly useful way of revealing inertial effects in dynamic tests. The stress in an elastic material is rate-independent. Thus, any differences between quasistatic and dynamic simulations of torsion on elastic specimens must necessarily be due to *inertial effects*: *gradients in stress and strain resulting from acceleration of the specimen*. As discussed above, axially nonuniform shear strains in the specimen would invalidate the analysis used to generate the stress-strain curves from the experimental data. Use of viscoelastic models in the simulations will add strain-rate effects but not alter the presence of inertial effects; as we will demonstrate, the main issue here is the slow shear wave speed in the specimen.

Finally, we emphasize that the purpose of this paper is not to propose or examine particular constitutive models for brain tissue or other soft materials but rather to investigate the validity of a particular dynamic test that was developed in an attempt to characterize the high strain-rate response of brain tissue.

The paper is organized as follows. First, in Section 2, we provide an overview of the loading pulses, material properties, and simulation parameters. Next, in Section 3, we discuss our one-dimensional analysis and simulations of torsional waves in a linear elastic specimen. In Section 4, we present the results of our quasistatic analysis and simulations of a full three-dimensional isotropic nonlinear elastic specimen. Here we used a compressible version of the well-known Mooney–Rivlin model for incompressible materials with bulk and shear moduli chosen to yield a nearly incompressible material. Section 5 contains the results of our three-dimensional dynamic simulations of the torsion test, most of which also used the Mooney–Rivlin model. However, Section 5B contains a brief summary of three-dimensional dynamic

simulations that used a nonlinear viscoelastic model for the specimen. Finally, Section 6 contains our major conclusions and their implications on the experimental data collected from torsional Kolsky bar tests. These should be relevant to other dynamic test techniques that attempt to generate a (locally) simple shear such as a double-lap shear test [Saraf et al. 2007; Trexler et al. 2011] or a circular shearing test [Nie et al. 2011]. In Appendix A, we provide some additional details of the numerical methods that were used. Appendix B contains the mathematical details of the loading pulses used in these simulations.

## 2. Overview of specimen properties, loading pulses, and simulations

We tailored our simulations to be relevant to the experimental loading conditions and specimen geometries considered in [Nie et al. 2013]. In Sections 2A–2C, we discuss how we arrived at our material parameters, boundary conditions, and loading pulse shapes. We also provide an overview of the set of simulations in Sections 2D and 2E.

**2A.** *Material properties.* From the 0.01/s and 1/s quasistatic tests on bovine brain tissue in [Nie et al. 2013], we estimated small strain shear moduli of $\mu = 4.5$ and 9 kPa, respectively.[1] In most of this paper, we use a shear modulus $\mu = 8$ kPa as representative of brain tissue.[2] This is near the upper limit of the quasistatic shear moduli reported for brain tissue in the literature, the lowest values being around 2 kPa [Donnelly and Medige 1997; Hrapko et al. 2006; Miller and Chinzei 1997; Nicolle et al. 2004; Saraf et al. 2007; Shuck and Advani 1972]. In view of the high water content of brain tissue, we assumed that the density of the brain tissue specimens was that of water (1 g/cm³). This specimen density was used in all simulations although the shear modulus was varied considerably (as described in Sections 2D and 2E).

**2B.** *Specimen geometry and boundary conditions.* The annular specimen was defined as a hollow cylinder of outer radius $R_o = 9.5$ mm, inner radius $R_i = 7.35$ mm, and relatively short length $L = 1.7$ mm, giving a small length-to-diameter ratio of 0.09.[3] Let $\bar{R}$ denote the arithmetic average radius and $\Delta$ the corresponding difference in radii:

$$\bar{R} = \frac{R_o + R_i}{2}, \qquad \Delta = \frac{R_o - R_i}{2} = R_o - \bar{R} = \bar{R} - R_i \tag{2-1}$$

so that $R_i = \bar{R} - \Delta$ and $R_o = \bar{R} + \Delta$. Table 1 summarizes the geometrical parameters for all of the simulations performed.

In the Kolsky bar tests, the faces of the specimen were glued to the incident bar and load cell, and for soft specimens, the twist at the specimen-load cell interface should be negligible compared to the twist at specimen-incident bar interface. Thus, for all simulations, one face of the annular specimen was subjected to a rigid rotation while the other face was fixed so that material points on either face could not undergo axial or radial displacements.

Relative to a cylindrical coordinate system, let $(r, \theta, z)$ and $(R, \Theta, Z)$ denote the coordinates of a material point in the deformed configuration and undeformed reference configuration, respectively. The

---

[1] In view of the difficulties in extracting an initial slope from stress-strain data, these estimates are reasonably close to their estimates of 5.9 and 10.4 kPa.

[2] An instantaneous elastic shear modulus of 40 kPa was used in the viscoelastic simulations discussed in Section 5B. The motivation for this choice is discussed there and in Section 3D.

[3] No information is provided in [Nie et al. 2013] as to the variability in specimen dimensions in the five samples they tested.

| $R_o$ (mm) | $R_i$ (mm) | $\bar{R}$ (mm) | $\Delta$ (mm) | $\Delta/\bar{R}$ | $L$ (mm) | $L/2R_o$ |
|---|---|---|---|---|---|---|
| 9.5 | 7.35 | 8.425 | 1.075 | 0.13 | 1.7 | 0.09 |

**Table 1.** Summary of geometrical parameters for all simulations conducted.

end of the specimen at $Z = L$ is taken to be the fixed face and thus corresponds to the specimen-load cell interface. The other end ($Z = 0$) corresponds to the specimen-incident bar interface; it is rotated by an angle $-\Psi(t)$, where $\Psi \geq 0$ is measured in radians and $t$ denotes time. Thus,

$$\theta|_{Z=0}(t) = \Theta - \Psi(t), \qquad \theta|_{Z=L}(t) = \Theta. \tag{2-2}$$

The *average angle of twist per unit length* is given by

$$\psi(t) = \frac{\theta|_{Z=L}(t) - \theta|_{Z=0}(t)}{L} = \frac{\Psi(t)}{L} \geq 0. \tag{2-3}$$

A measure of the *average shear strain-rate in the specimen* often used in the experimental literature on torsional Kolsky bar tests is

$$\dot{\gamma}_{\mathrm{s}}(t) = \frac{\dot{\theta}|_{Z=L}(t) - \dot{\theta}|_{Z=0}(t)}{L}\bar{R} = \frac{\dot{\Psi}(t)}{L}\bar{R} = \dot{\psi}(t)\bar{R}, \tag{2-4}$$

where a superposed dot denotes the time derivative and $\bar{R}$ is the average radius introduced above [Gilat 2000; Nie et al. 2013]. This average shear strain-rate is typically inferred from strain gage measurements on the bar(s) and then integrated to give an *average shear strain in the specimen*:

$$\gamma_{\mathrm{s}}(t) = \frac{\theta|_{Z=L}(t) - \theta|_{Z=0}(t)}{L}\bar{R} = \frac{\Psi(t)}{L}\bar{R} = \psi(t)\bar{R} \geq 0. \tag{2-5}$$

While other measures of average shear strain are often used in the theoretical literature (see Section 4B), we will use $\gamma_{\mathrm{s}}(t)$ and its rate in order to simplify comparison with the experimental data in [Nie et al. 2013]. For the dynamic simulations considered here, we applied an angular displacement at $Z = 0$ that delivered the desired average strain-rate history $\dot{\gamma}_{\mathrm{s}}(t)$ for the particular simulation. In view of (2-2) and (2-5), this displacement history is given by

$$\theta|_{Z=0}(t) - \Theta = -\Psi(t) = -\frac{L}{\bar{R}}\gamma_{\mathrm{s}}(t). \tag{2-6}$$

**2C. *Loading pulse shapes.*** We use the term *loading pulse* to refer to the average strain-rate history imposed on the specimen. The key features of a typical loading pulse[4] are summarized in panel *a* of Figure 2. These loading pulses are intended to mimic those generated in Kolsky bar experiments. The pulse ramps up smoothly over the time interval $[0, t_r]$ to a maximum average strain-rate $\dot{\gamma}_{\max}$, which is held constant for the plateau duration $t_p$. We assume a symmetric unloading of the pulse; that is, the unloading time is equal to the rise time $t_r$ so that the total duration $t_d$ of the loading pulse is given by

$$t_d = 2t_r + t_p. \tag{2-7}$$

The average strain accumulated during the constant strain-rate portion is $t_p\dot{\gamma}_{\max}$. For the loading pulse shapes considered here, the strains  accumulated during the initial rise and during the unloading are

---

[4] A complete mathematical description of this idealized loading pulse is included in Appendix B.
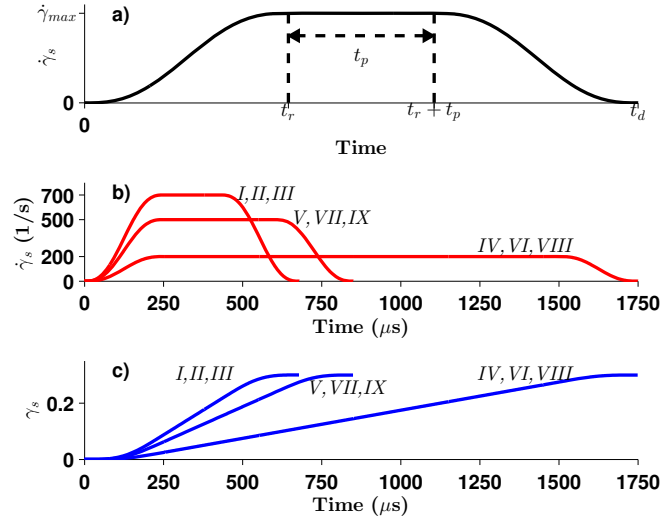
**Figure 2.** Key features of a typical average strain-rate history for the dynamic simulations (panel *a*). Average strain-rate histories (panel *b*) and strain histories (panel *c*) for *Simulations I–IX*.

each $\frac{1}{2}t_r\dot{\gamma}_{\max}$. Thus, the total average strain is

$$\gamma_{\max} = 2\left(\tfrac{1}{2}t_r\dot{\gamma}_{\max}\right) + t_p\dot{\gamma}_{\max} = (t_r + t_p)\dot{\gamma}_{\max}. \tag{2-8}$$

Nie et al. [2013] reported stress-strain curves from quasistatic and torsional Kolsky bar tests on five samples of bovine brain tissue. The Kolsky bar tests in [Nie et al. 2013] are described as being at a strain-rate of 700/s with a pulse duration of 600 $\mu$s. The final average shear strain for their tests was about 0.3. No additional details of the loading pulse are provided with the following exception. The reader is referred to their Figure 4 for "a typical set of Kolsky torsion bar result". This figure has plots of output voltage versus time for the two gages. The only information that we could infer from this figure is that the rise time of the loading pulse shown was about 250 $\mu$s.[5]

An *average* strain-rate history $\dot{\gamma}_s(t)$ consistent with the key features described above was obtained by choosing the imposed maximum (average) strain-rate $\dot{\gamma}_{\max}$ to be 700/s, the rise time $t_r$ to this 700/s plateau to be 250 $\mu$s, and the maximum (average) strain $\gamma_{\max}$ to be 0.3. These conditions, together with (2-7) and (2-8), yield a plateau duration of $t_p = 179\,\mu$s and a loading pulse duration of $t_d = 679\,\mu$s. The curves for the one-dimensional *Simulations I–III* in Figure 2 show the average strain-rate history $\dot{\gamma}_s(t)$ (panel *b*) and the corresponding average strain history $\gamma_s(t)$ (panel *c*) obtained from this construction. The other two curves in these panels are the average strain and strain-rate histories for the one-dimensional *Simulations V, VII,* and *IX* and *Simulations IV, VI,* and *VIII*.

---

[5] From the discussion in [Nie et al. 2013], it is not clear whether the data in this figure corresponds to any of the tests in that paper or whether the data is taken from an earlier study by Nie et al. [2011] that is cited frequently in the 2013 paper. The earlier paper describes a *circular shearing test*, but it is referred to as a torsion test. Results from that paper are cited as providing evidence that the specimens were "undergoing uniform deformation" for the 700/s tests in [Nie et al. 2013], a claim that is contradicted by the results presented here.

| parameter | unit | Simulation | | | | | | | | |
|---|---|---|---|---|---|---|---|---|---|---|
| | | *I* | *II* | *III* | *IV* | *V* | *VI* | *VII* | *VIII* | *IX* |
| $\gamma_{\max}$ | | 0.3 | — | — | — | — | — | — | — | — |
| $\dot{\gamma}_{\max}$ | 1/s | 700 | 700 | 700 | 200 | 500 | 200 | 500 | 200 | 500 |
| $t_r$ | $\mu$s | 250 | — | — | — | — | — | — | — | — |
| $t_p$ | $\mu$s | 179 | 179 | 179 | 1250 | 350 | 1250 | 350 | 1250 | 350 |
| $t_d$ | $\mu$s | 679 | 679 | 679 | 1750 | 850 | 1750 | 850 | 1750 | 850 |
| $\rho$ | g/cm$^3$ | 1 | — | — | — | — | — | — | — | — |
| $\mu$ | kPa | 800 | 80 | 8 | 8 | 8 | 80 | 80 | 800 | 800 |
| $c$ | mm/$\mu$s | 0.0283 | 0.0089 | 0.0028 | 0.0028 | 0.0028 | 0.0089 | 0.0089 | 0.0283 | 0.0283 |
| $t_{\text{travel}}$ | $\mu$s | 60.1 | 190.1 | 601 | 601 | 601 | 190.1 | 190.1 | 60.1 | 60.1 |

**Table 2.** Summary of material and loading pulse parameters for nine one-dimensional simulations. Long dashes (—) indicate parameters that were not changed.

## 2D. *One-dimensional torsion simulations.*

The one-dimensional linear elastic simulations described in Sections 3C, 3D, and 3F were conducted with the primary focus on the effects of the shear modulus and the loading pulse on the quality of the experiment. Table 2 summarizes the parameters specific to the nine one-dimensional simulations in Sections 3C and 3D. Columns 1 and 2 list the parameters and respective units, and the remaining columns give the values of the parameter used. The shear modulus was varied by two orders of magnitude: 800, 80, and 8 kPa, the latter being on the order of brain tissue, as discussed in Section 2A. These shear moduli are used in *Simulations I, II,* and *III*, respectively, together with the 700/s loading pulse discussed above. In Section 3C, the spatial and temporal variation of the actual shear strain and shear strain-rate in the specimen are compared for these three simulations.

In Section 3D, we compare the "stress-strain curves" for the same three shear moduli and three maximum (average) strain-rates (200, 500, and 700/s) for a total of nine simulations (*Simulations I–IX*). The 200/s and 500/s loading pulses had the same rise time (250 $\mu$s) and maximum strain (0.3) as the 700/s case but different plateau durations and total pulse durations (see Table 2 and Figure 2). The "stress-strain curves" presented here are obtained by plotting the average shear stress at the load cell versus the average shear strain in the specimen as in the experimental results reported by [Nie et al. 2013]. The errors introduced by this procedure are illustrated by comparison with the actual (linear) stress-strain curves that would have been obtained if the specimen were undergoing a uniform (i.e., pure torsional) deformation.

In Section 3F, we explore the plausibility of improving the quality of experimental results by changing the parameters of the loading pulse, specifically the rise time $t_r$ and plateau duration $t_p$. In these studies, $t_r$ took on the thirteen values 125, 250, 500, 750, 1000, 1250, 1500, 1750, 2000, 2250, 2500, 2750, and 3000 $\mu$s and $t_p$ took on the eleven values 1, 100, 200, 300, 400, 500, 600, 700, 800, 900, and 1000 $\mu$s for a total of 143 additional one-dimensional simulations. These simulations were conducted on a soft material with the same geometry and material properties as in *Simulation III*.

Additional details about the numerical methods for the one-dimensional simulations are included in Appendix A.

## 2E. *Three-dimensional torsion simulations.*

In all of our three-dimensional simulations, stress-free boundary conditions were used on the outer surface $R = R_o$ and the inner surface $R = R_i$ of the annular specimen. With the exception of the viscoelastic results in Section 5B, the constitutive relation for the

specimen was a compressible version of the nonlinear elastic Mooney–Rivlin model (see Section 4). We used a bulk modulus of 2.3 GPa for all simulations; this is the bulk modulus of water and approximates the bulk modulus of many gelatins and soft tissues (such as brain tissue).

For the quasistatic simulations in Section 4F, the shear modulus was varied by almost three orders of magnitude: $\mu = 800$, 80, 8, and 2 kPa. The corresponding ratios of bulk to shear modulus varied from 2875 to $1.15 \times 10^6$ so that in all cases the material was nearly incompressible. For each value of the shear modulus, simulations were performed for three values of the nondimensional parameter $\omega$ in the Mooney–Rivlin model: 0.3, 0.6, and 1 (neo-Hookean model).

The three-dimensional dynamic simulations (*Simulations X–XVIII*) with an elastic specimen are discussed in Section 5A. The material parameters for these simulations were varied in an analogous way to the three-dimensional quasistatic simulations except that the $\mu = 2$ kPa case was not considered. The loading parameters were the same as in the one-dimensional *Simulations I–III*. Section 5B contains a brief discussion of some three-dimensional dynamic simulations that used a nonlinear viscoelastic model for the specimen.

Additional details about the numerical methods for both the quasistatic and dynamic three-dimensional simulations are included in Appendix A.

## 3. One-dimensional treatment of dynamic torsion

Unlike traditional Kolsky bar tests where the force or torque is measured at both ends of the specimen, in the modified torsional Kolsky bar test of [Nie et al. 2013], the torque is measured by a load cell at one end of the specimen only, and a (radially averaged) shear stress *at that end of the specimen* is extracted from this measurement. The test provides no means for determining whether an axially uniform state of shear stress has been achieved in the specimen. This would not be an issue if the shear strain could also be measured at the specimen-load cell interface, in which case a valid stress-strain curve could be obtained. However, it is not possible to measure the shear strain at any specific location in the specimen. Only an average measure of shear strain in the specimen, $\gamma_s(t)$ in (2-5), can be extracted from the test data, and this represents a volumetric average.[6]

As pointed out in the introduction, the stress-strain curves reported by [Nie et al. 2013] were obtained by plotting the (radially averaged) shear stress at the load cell versus the average shear strain $\gamma_s(t)$ in the specimen. Clearly, this is meaningful only if $\gamma_s(t)$ is close to the actual shear strain at the specimen-load cell interface. Such a condition can be expected to hold over some time interval only if the shear strain in the specimen is axially uniform on that time interval. In an effort to determine when a state of uniform shear strain can be achieved, we have performed one-dimensional simulations of dynamic torsion on linear elastic specimens. Although the goal of the torsional Kolsky bar tests is to measure strain-rate effects due to viscoelastic properties of the material, a study of one-dimensional linear elastic wave propagation in the torsion specimens reveals the difficulty in achieving uniform conditions in soft specimens.

In Section 3A, we discuss the one-dimensional wave equation that is solved in our simulations. Section 3B contains a brief discussion of dynamic equilibrium. An overview of the simulations in Sections 3C, 3D, and 3F was given in Section 2D. In Section 3E, we consider some ways of improving the quality of the torsion experiments.

---

[6] In this regard, see also (3-11) below.

**3A.** *The wave equation for dynamic torsion.* To investigate the possibility of axially nonuniform shear strains in dynamic torsion tests, we consider the torsional deformation

$$r = R, \qquad \theta = \theta(Z, t) = \Theta + \delta(Z, t), \qquad z = Z \tag{3-1}$$

so that

$$\delta(z, t) \equiv \theta(z, t) - \Theta \tag{3-2}$$

is the angular displacement at the axial location $z$ at time $t$. Note that for the deformation (3-1) there are no axial or radial displacements in the specimen. The boundary conditions (2-2) imply that the angular displacements at the ends of the specimen are

$$\delta(L, t) = 0, \qquad \delta(0, t) = \theta(0, t) - \Theta = -\Psi(t) = -L\psi(t). \tag{3-3}$$

Recall that $\psi(t)$ is the *average* angle of twist per unit length (see (2-3)).

We assume that the displacement vector $\boldsymbol{u}$ and its spatial gradient $\nabla \boldsymbol{u}$ are infinitesimal. Let $\boldsymbol{\epsilon}$ denote the infinitesimal strain tensor: $\boldsymbol{\epsilon} = \frac{1}{2}(\nabla \boldsymbol{u} + (\nabla \boldsymbol{u})^T)$. Then for the deformation (3-1), the only nonzero components[7] of $\boldsymbol{u}$ and $\boldsymbol{\epsilon}$ relative to the cylindrical coordinate system are

$$u_\theta = r\delta(z, t), \qquad \epsilon_{z\theta} = \epsilon_{\theta z} = \frac{1}{2}\frac{\partial u_\theta}{\partial z} = \frac{1}{2}r\frac{\partial \delta}{\partial z}. \tag{3-4}$$

We also assume that the specimen satisfies the isotropic linear elastic constitutive relation

$$\boldsymbol{T} = \lambda(\mathrm{tr}\,\boldsymbol{\epsilon})\boldsymbol{I} + 2\mu\boldsymbol{\epsilon}, \tag{3-5}$$

where $\boldsymbol{T}$ is the Cauchy stress tensor and the constants $\lambda$ and $\mu$ are the Lame modulus and shear modulus, respectively. Then for the deformation (3-1), the only nonzero components of $\boldsymbol{T}$ are

$$T_{z\theta} = T_{\theta z} = 2\mu\epsilon_{\theta z} = \mu\frac{\partial u_\theta}{\partial z} = \mu r\frac{\partial \delta}{\partial z}. \tag{3-6}$$

In this case, the equations for momentum balance in cylindrical coordinates reduce to

$$\frac{\partial T_{\theta z}}{\partial z} = \rho\frac{\partial^2 u_\theta}{\partial t^2}, \tag{3-7}$$

where $\rho$ is the specimen density. Then by (3-6), it follows that $u_\theta$ satisfies the one-dimensional wave equation; hence, by (3-4)$_1$ and (3-2), $\delta$ and $\theta$ satisfy the same equation.[8] For example,

$$\frac{\partial^2 \delta}{\partial t^2} = c^2\frac{\partial^2 \delta}{\partial z^2}, \qquad c = \sqrt{\frac{\mu}{\rho}}. \tag{3-8}$$

That is, a small angular displacement will propagate axially along the specimen at the linear elastic shear wave speed $c$.[9]

---

[7] Here and elsewhere in the paper, we use the physical components of vectors and tensors, that is, their components relative to the unit basis vectors along the cylindrical coordinate directions. See [Graff 1975, §A.9.1] for the physical components of $\boldsymbol{\epsilon}$ and the momentum balance equations for infinitesimal strains.

[8] These results also follow from strength-of-materials approximations [Graff 1975, §2.6; Wylie 1975, §8.2].

[9] A shear wave propagating into an initially unstrained, *nonlinear* elastic material also travels at the linear elastic wave speed [Truesdell and Noll 1965, §73, 74, 77]. The shear wave speed may change after the wave is reflected and begins to travel into

The results above hold for both disc-shaped specimens and annular specimens.[10] In either case, the outer lateral surface $r = R_o$, and for annular specimens the inner lateral surface $r = R_i$, is stress-free since $T_{rr} = T_{r\theta} = T_{rz} = 0$. The shear strain $\epsilon_{\theta z}$ and the shear stress $T_{\theta z}$ vary linearly with the radius as shown above. Restricting attention to annular specimens, we see from (3-6) that the arithmetic average of the shear stress at the outer and inner lateral surfaces is

$$\sigma(z, t) \equiv \frac{T_{\theta z}|_{r=R_o} + T_{\theta z}|_{r=R_i}}{2} = \mu \bar{R} \frac{\partial \delta}{\partial z} = \mu \gamma(z, t), \tag{3-9}$$

where

$$\gamma(z, t) \equiv \bar{R} \frac{\partial \delta}{\partial z} = \bar{R} \frac{\partial \theta}{\partial z}. \tag{3-10}$$

Note that, by (3-4), $\gamma(z, t)$ is twice the arithmetic average of $\epsilon_{\theta z}(z, t)$ at the outer and inner lateral surfaces.[11] In interpreting the results of our one-dimensional simulations, we have chosen to use $\gamma(z, t)$ as a measure of the *radially averaged* shear strain at the axial location $z$ for consistency with the average shear strain $\gamma_s(t)$ used in the experimental literature. Indeed, by (3-10), (3-3), and (2-5), $\gamma_s(t)$ is the axial average value of $\gamma(z, t)$:

$$\frac{1}{L} \int_0^L \gamma(z, t) \, dz = \frac{1}{L} \int_0^L \bar{R} \frac{\partial \delta}{\partial z} \, dz = \frac{\bar{R}}{L} [\delta(L, t) - \delta(0, t)] = \psi(t) \bar{R}$$

$$= \gamma_s(t). \tag{3-11}$$

Note that since $\gamma(z, t)$ represents a radial average of the shear strain at $z$, $\gamma_s(t)$ represents a volumetric average of the shear strain in the specimen.

Recall that, in the dynamic torsion tests, the angle of twist $\Psi(t)$ imparted to the face of the specimen (at $z = 0$) is typically determined in such a way that a desired average strain-rate history $\dot{\gamma}_s(t)$ is delivered. By (3-2) and (2-6), the angular displacement history necessary to deliver that average strain-rate history is

$$\delta(0, t) = -\frac{L}{\bar{R}} \gamma_s(t). \tag{3-12}$$

The average strain histories shown in Figure 2c, when substituted into (3-12), yield the angular displacement boundary conditions that are actually applied at the loading end of the specimen ($z = 0$) in our simulations. These simulations involve the numerical solution[12] of the one-dimensional wave equation (3-8) for $\delta$ with zero initial conditions and boundary conditions (3-12) and (3-3)$_1$ (i.e., $\delta(L, t) = 0$).

A *pure torsional deformation* satisfying the boundary conditions (2-2) is given by (3-1) with angular displacement

$$\delta(z, t) = \psi(t)(z - L), \quad \psi \geq 0. \tag{3-13}$$

---

a strained portion of the material. For the strains considered here, nonlinearity could introduce small variations in wave speeds that would be minor compared with other effects discussed later.

[10] Because of the small length-to-diameter ratio of the specimens considered here, namely 0.09, the more common terms "rod" and "tube" do not seem appropriate.

[11] For the annular specimens considered here, the shear strain should be approximately radially uniform. See the discussion of pure torsional deformation in Section 4B.

[12] Additional details about the numerical methods for the one-dimensional simulations are included in Appendix A.

In this case, by (3-4), the only nonzero components of the infinitesimal strain tensor are

$$\epsilon_{z\theta} = \epsilon_{\theta z} = \tfrac{1}{2}\psi(t)r \geq 0. \tag{3-14}$$

And by (3-10) and (2-5), the shear strain $\gamma$ is axially uniform and equal to the average shear strain $\gamma_s$:

$$\gamma(z, t) = \psi(t)\bar{R} = \gamma_s(t) \quad \text{for pure torsion.} \tag{3-15}$$

*However, a state of pure torsion might not be achieved in a given test so that $\gamma(z, t) \neq \gamma_s(t)$ in general.* The degree to which $\gamma(z, t)$ differs from its measured average value $\gamma_s(t)$ is a critical point of this paper and is discussed in the following sections.

**3B.** *Dynamic equilibrium.*  In the experimental literature, the terms "force equilibrium", "stress equilibrium", "dynamic stress equilibrium", or simply "dynamic equilibrium" are used to indicate that the axial forces (compression tests) or torques (torsion tests) on the two ends of the specimen are balanced [Gray 2000; Chen and Song 2011]. This condition is clearly necessary (but not sufficient) for an axially uniform state of stress and strain within the specimen, and in the experimental literature, these uniform conditions are often (implicitly) assumed to hold on any time interval for which dynamic equilibrium is achieved. We will use the term "dynamic equilibrium" in this stronger sense of axially uniform stress and strain states.

Whether or not dynamic equilibrium is reached depends on many factors, including the properties of the loading pulse, the specimen wave speed, and the specimen length. In particular, a critical factor in achieving dynamic equilibrium in torsion tests is the travel time of the shear wave:

$$t_{\text{travel}} = \frac{L}{c} = L\sqrt{\frac{\rho}{\mu}}, \tag{3-16}$$

that is, the time it takes for the shear wave to travel from one end of the specimen to the other. For a uniform strain state to exist in the material, key features of the loading pulse such as the rise time $t_r$ and the plateau duration $t_p$ need to be much longer than the travel time to allow the specimen to "ring-up" to dynamic equilibrium after multiple reflections.

Table 2 lists the three different travel times for *Simulations I–IX*; recall that we assume the density $\rho$ is that of water and the specimen length $L$ is 1.7 mm. For the values of the shear modulus used in our dynamic simulations (8–800 kPa), the travel time ranges from 601 $\mu$s to 60.1 $\mu$s. Since the travel time is the delay in microseconds between the initial loading of the specimen at $z = 0$ and the arrival of the wave at the load cell at $z = L$, the way this travel time is incorporated into the analysis of experimental data is extremely important when generating stress-strain curves as we will demonstrate in Section 3D. Assuming that the shear stress $\sigma(L, t)$ at the load cell is being plotted against the measured averaged shear strain $\gamma_s(t)$, these signals would have to be shifted in time to synchronize them. However, we will show that this procedure can introduce considerable errors.

**3C.** *Failure of soft specimens to reach equilibrium.*  In this section, we examine the spatial and temporal variation of the strain and strain-rate in the specimen for *Simulations I–III*. These simulations differ only in the value of the shear modulus $\mu$ used for the specimen (see Table 2). The results are summarized in Figure 3. False color images of the strain-rate (left panels) and strain (right panels) as a function of axial
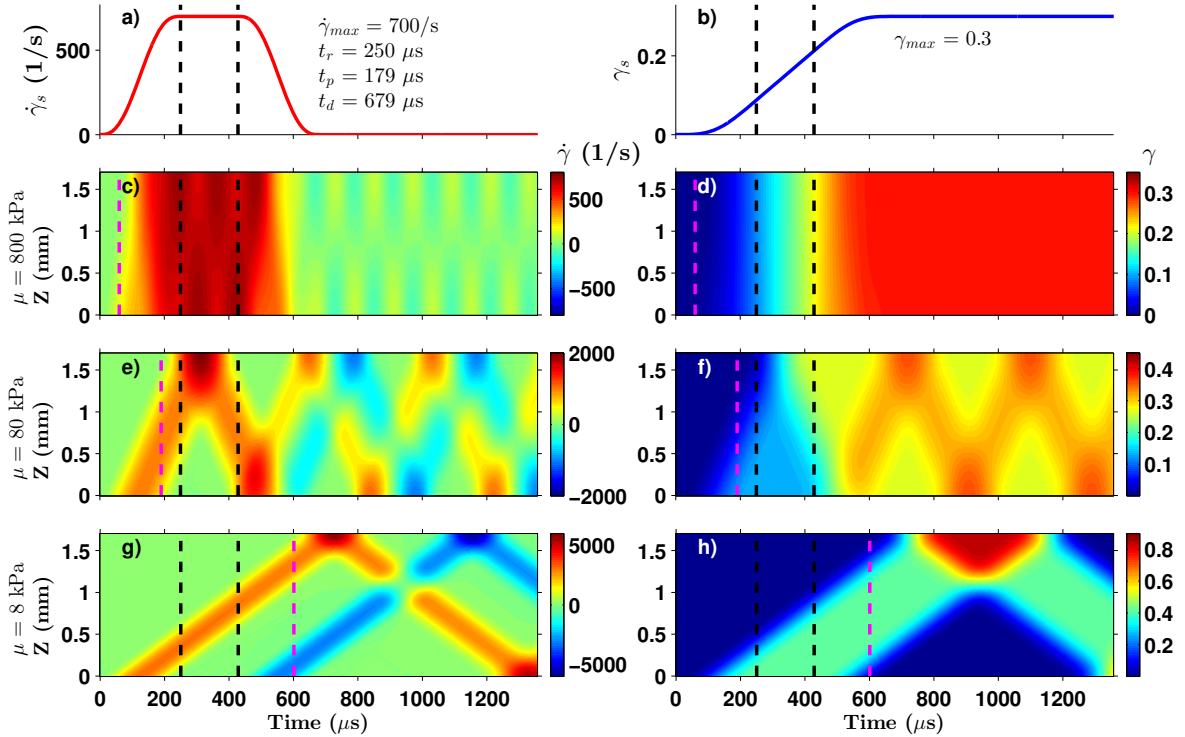
**Figure 3.** The average strain-rate history $\dot{\gamma}_s(t)$ (panel $a$) and corresponding average strain history $\gamma_s(t)$ (panel $b$) imposed on the specimen for *Simulations I–III*. The first black vertical dashed line corresponds to the rise time $t_r$ to constant strain-rate. The second black vertical dashed line is the time ($t_r + t_p$) at which the strain-rate starts to ramp down after a constant strain-rate plateau of duration $t_p$. The remaining panel pairs ($c$–$d$, $e$–$f$, and $g$–$h$) are false color images of the corresponding actual strain-rates $\dot{\gamma}(z, t)$ and strains $\gamma(z, t)$ in specimens with shear moduli $\mu = 800$, 80, and 8 kPa, respectively. Note that the color scale varies for the three groups of plots. The vertical magenta lines correspond to $t_{\text{travel}}$, which depends on the shear modulus.

position (vertical axis) and time are presented in panels $c$–$h$. Panels $a$ and $b$ show the *average* strain-rate and strain histories that are imposed on the specimen.

Figure 3 illustrates the degree to which dynamic equilibrium has (or has not) been achieved. Shear waves are initiated at the specimen–bar interface ($z = 0$) and propagate to the *Load Cell* ($z = L$). In each panel, the first vertical black dashed line indicates the rise time $t_r$. The two vertical black dashed lines taken together represent the window of time during which the imposed average strain-rate is constant. The vertical magenta dashed line indicates the travel time and thus the arrival of the shear wave at the *Load Cell*, which increases with decreasing shear modulus (see (3-16)). Thus, the black dashed lines indicate the key time scales of the loading pulse and the magenta line represents the critical travel time of the specimen. Ideally, the magenta line should lie well before both black lines.

The results for $\mu = 800$ kPa (*Simulation I*) are shown in panels $c$ and $d$ of Figure 3. These results are close to what one might expect for a valid torsional Kolsky bar experiment. The strain-rate (panel $c$)

increases to an approximately axially uniform (intended) plateau value of 700/s before dropping back down to a zero strain-rate but nonzero final strain (panel *d*). From the false-color representation, one can conclude that both the strain and strain-rate are fairly uniform along the length of the specimen at any instant. This is indicated by a nearly uniform color in the vertical direction at any instant. The ringing that can be seen, especially in the strain-rate, is one of the fundamental modes of the specimen. There is moderate variability in the strain-rate due to the ringing, but the intended strain-rate and maximum strain nearly match their imposed average values plotted in panels *a* and *b*. Thus, panels *c* and *d* in Figure 3 are a representation of a strain state where dynamic equilibrium is nearly achieved. If dynamic equilibrium was actually reached, the color representation of $\gamma(z, t)$ and $\dot{\gamma}(z, t)$ would not change in the vertical direction.

The results for the smaller shear modulus, $\mu = 8$ kPa (*Simulation III*), are shown in panels *g* and *h* of Figure 3. Clearly, the strain and strain-rate in *Simulations III* and *I* are considerably different both in magnitude and uniformity. Recall that a shear modulus of 8 kPa is on the order of brain tissue, so the specimen stiffness in this case most closely resembles the stiffness of the brain tissue specimens in the tests of [Nie et al. 2013]. Since the linear elastic shear wave speed is proportional to the square root of the shear modulus and the shear modulus in *Simulation III* is one hundred times smaller than in *Simulation I*, the wave speed is ten times slower than in *Simulation I*. The travel time is therefore ten times longer, i.e., 601 $\mu$s instead of 60 $\mu$s (compare the magenta lines for panels *c* and *d* against panels *g* and *h* in Figure 3). For the $\mu = 8$ kPa case, the travel time is so close to the pulse duration ($t_d = 679\,\mu$s) that the shear strain and shear strain-rate within the specimen are nonuniform traveling pulses. Thus, *the same loading conditions* that produced axially uniform shear strain and shear strain-rate in the $\mu = 800$ kPa case resulted in highly nonuniform shear strain and shear strain-rate within the 8 kPa specimen.

For the $\mu = 8$ kPa case, it is grossly inaccurate to describe the strain and strain-rate at any location in the specimen by their average values $\gamma_s$ and $\dot{\gamma}_s$ although these averages are all that can be inferred from test measurements. The following features illustrate the degree of nonuniformity in the specimen:

(1) During the first 600 $\mu$s of the simulation, that is, prior to reflection of the shear wave from the *Load Cell*, the peak strain-rate and peak strain in the specimen are about 3200/s and 0.42, respectively. These peak values occur at different axial locations at different times (see panels *g* and *h*) and well exceed the maximum average strain-rate ($\dot{\gamma}_{\max} = 700$/s) and maximum average strain ($\gamma_{\max} = 0.3$).

(2) The largest strain achieved in the specimen during the simulation is about 0.84. This occurs near the end $Z = 1.7$ mm (i.e., adjacent to the *Load Cell*) at about 900 $\mu$s (panel *h*). This peak strain is nearly three times larger than the average strain $\gamma_s$ at 900 $\mu$s, which has already reached its final value of $\gamma_{\max} = 0.3$.

(3) The largest strain-rate achieved in the specimen during the simulation is about 5800/s. This also occurs at the *Load Cell* end of the specimen ($Z = 1.7$ mm) at about 730 $\mu$s, by which time the average strain-rate $\dot{\gamma}_s$ has unloaded to zero. This peak strain-rate is more than eight times higher than the maximum average strain-rate (700/s) imposed on the specimen.

(4) Large positive strain-rates and a zero *average* strain-rate at the same instant imply negative strain-rates of large absolute value must also be experienced in some portions of the specimen. This is evidenced by the blue bands in panel *g*.

(5) The doubling of the peak strains (from 0.42 to 0.84) and the near doubling of the peak strain-rates

(from 3200/s to 5800/s) is due to the reflection of the shear wave from the fixed end ($Z = 1.7$ mm) beginning at 601 $\mu$s.[13]

(6) As an example of the large axial gradients, the strain at 300 $\mu$s decreases from 0.275 to 0 over a distance of 0.3 mm. However, the change in the angle of twist over this 0.3 mm length is quite small: roughly 0.005 radians or about $0.3°$. This is well below the resolution of the high speed camera images of the specimen in [Nie et al. 2011] that were often cited in [Nie et al. 2013] as evidence that the specimens undergo uniform deformation.

The results for $\mu = 80$ kPa (*Simulation I*) are shown in panels $e$ and $f$ of Figure 3. Even for this intermediate case, dynamic equilibrium is not reached. Further evidence of this fact is given by the stress-strain curves for $\mu = 80$ kPa in the next section. Clearly, achieving dynamic equilibrium in specimens with shear moduli substantially less than 800 kPa can be quite problematic.

**3D.** ***"Stress-strain curves" for linear elastic specimens.*** Up to this point, we have used the linear elastic simulations only for predictions of the strain and strain-rate within the specimen. In this section, we use the results of those simulations to construct "stress-strain curves" at several "constant strain-rates", analogous to the way that test data is typically analyzed and presented in the experimental literature.

Let $\sigma_{\text{Load Cell}}(t)$ and $\gamma_{\text{Load Cell}}(t)$ denote the (radially averaged) shear stress and shear strain at the *Load Cell*:

$$\sigma_{\text{Load Cell}}(t) = \sigma(L, t), \qquad \gamma_{\text{Load Cell}}(t) = \gamma(L, t). \tag{3-17}$$

In the torsional Kolsky bar test of [Nie et al. 2013], the torque is measured at the load cell and $\sigma_{\text{Load Cell}}(t)$ can be extracted from this measurement. However, $\gamma_{\text{Load Cell}}(t)$ cannot be measured in this or any other torsional Kolsky bar test — only the average shear strain $\gamma_s(t)$ can be inferred as discussed in Section 2B. Consequently, the stress-strain curves in [Nie et al. 2013] are plots of $\sigma_{\text{Load Cell}}$ versus $\gamma_s$. But while $\gamma_s(t)$ starts increasing at $t = 0$, that is, as soon as the twist is applied to the end $z = 0$, there is a delay (equal to the travel time) before a nonzero strain is experienced by the specimen at the load cell (see Figure 3). Since this travel time is a significant portion of the test duration for the soft specimens of interest, it might seem reasonable to time-shift the $\sigma_{\text{Load Cell}}(t)$ history in order to synchronize it with the $\gamma_s(t)$ history (or vice versa) prior to plotting one against the other. On the other hand, *a time shift is unnecessary if the specimen is in dynamic equilibrium*, a condition that Nie et al. [2013] assumed to hold in their tests. Since the issue of travel time in the specimen was not discussed in their paper, it was not clear to us whether a time shift had been performed in generating their stress-strain curves.

In this section, we utilize the results from *Simulations I–IX* (see Table 2) to generate "stress-strain curves" (i.e., $\sigma_{\text{Load Cell}}$ versus $\gamma_s$) with and without time shifts. We compare the results of both approaches in order to illustrate the different apparent "strain-rate effects" that each produces. Recall that the simulations solve the one-dimensional wave equation (3-8) for the angular displacement $\delta$ with the boundary condition at $z = 0$ determined by the appropriate average strain history (see (3-12) and Figure 2). Six sets of "stress-strain curves" are plotted in Figure 4. Solid colored curves are shear stress measured at the *Load Cell* plotted against the average shear strain $\gamma_s$. The colored curves in the left column do not involve any time shifts of the data; i.e., they are parametric plots of $\sigma_{\text{Load Cell}}(t)$ versus $\gamma_s(t)$. The colored

---

[13] Another doubling would be expected to occur at the specimen-bar interface ($Z = 0$) if the simulation had been continued to longer times.

curves in the right column are parametric plots of $\sigma_{\text{Load Cell}}(t - t_{\text{travel}})$ versus $\gamma_s(t)$; i.e., the *Load Cell* data has been time-shifted to synchronize it with the average strain data. Each row of plots is for a unique shear modulus (800, 80, and 8 kPa), and each color within a panel represents a simulation taken at a different intended maximum *average* strain-rate: $\dot{\gamma}_{\text{max}} = 700/\text{s}$ (blue), $500/\text{s}$ (green), and $200/\text{s}$ (red). The average strain-rate histories are shown in panel *b* of Figure 2. The maximum strain $\gamma_{\text{max}}$ and rise time were held constant at 0.3 and $250\,\mu\text{s}$, respectively, and only the plateau time and the total duration were changed to accommodate the various strain-rates (see Table 2).

In the simulations the stress and strain at the *Load Cell* are linearly related: setting $z = L$ in (3-9) gives

$$\sigma_{\text{Load Cell}}(t) = \mu \gamma_{\text{Load Cell}}(t). \tag{3-18}$$

*Thus, regardless of the strain and strain-rate histories experienced by the specimen, a parametric plot of $\sigma_{\text{Load Cell}}(t)$ versus $\gamma_{\text{Load Cell}}(t)$ should be linear with slope $\mu$.* We cannot actually plot the linear relation in (3-18) in Figure 4 since the variable on the horizontal axis is $\gamma_s(t)$, which (as shown in Section 3C) is generally not equal to $\gamma_{\text{Load Cell}}(t)$. However, if the shear strain were uniform, then $\gamma_s$ would coincide with $\gamma_{\text{Load Cell}}$, in which case the shear stress at the *Load Cell* would vary linearly with $\gamma_s$: $\sigma_{\text{Load Cell}} = \mu \gamma_s$. This linear curve is shown by the black dashed lines in each panel in Figure 4. It represents *the correct stress-strain curve* against which the colored "rate-dependent" curves should be compared. That is, while each of the colored curves are valid plots of $\sigma_{\text{Load Cell}}$ versus $\gamma_s$ (with or without time shifts), they represent the $\sigma_{\text{Load Cell}}$ versus $\gamma_{\text{Load Cell}}$ curve only to the extent to which they agree with the black dashed lines in Figure 4. Recall that the shear strain $\gamma(z, t)$ is uniform for a specimen undergoing a pure torsional deformation (see the discussion at the end of Section 3A). Hence, the black dashed lines represent the stress-strain curves that would be obtained for pure torsion.

Panel *a* in Figure 4 corresponds to a shear modulus of 800 kPa without a time shift. Note that all four curves lie nearly on top of each other. Here the blue curve represents the results from *Simulation I*. As discussed earlier, this was considered a "valid" Kolsky bar test, and that conclusion is confirmed here. Panel *b* is the same set of stresses shifted by the travel time ($60\,\mu\text{s}$). This has the *appearance* of valid Kolsky bar data. Note, however, that all these curves are vertically offset from the true (dashed) response, implying an apparent rate-dependence. Despite the vertical offset, their slopes capture the true linear behavior of the material.

*We emphasize that if a linear elastic specimen is in dynamic equilibrium, there should be absolutely no strain-rate effects.* However, Figure 4 clearly shows that, for the smaller shear moduli of 80 and 8 kPa, the apparent "rate effects" are substantial regardless of whether the *Load Cell* data is time-shifted. It is unclear what information could have been inferred from these plots if the true linear stress-strain relation were unknown with the exception that, for $\mu = 80$ kPa, a linear fit to the unshifted curves or to the time-shifted 200/s curve might return a slope close to $\mu$.

When the shear stress is plotted without a time shift, there is an initial strain interval for which the stress is zero. The strain duration of this initially flat portion of the stress-strain curve increases with the strain-rate and decreases with increasing shear modulus. These initially flat regions are present even for the $\mu = 800$ kPa case (panel *a*) although they cannot be observed on the scale of that figure. This nonphysical behavior is most profound for the softest specimen ($\mu = 8$ kPa, panel *e*). In particular, for the 700/s case in that panel, there is no measured stress until $\gamma_s(t)$ is close to 0.3. Recall that it takes $601\,\mu\text{s}$ for the shear wave to arrive at *Load Cell* whereas the average strain has reached its final value
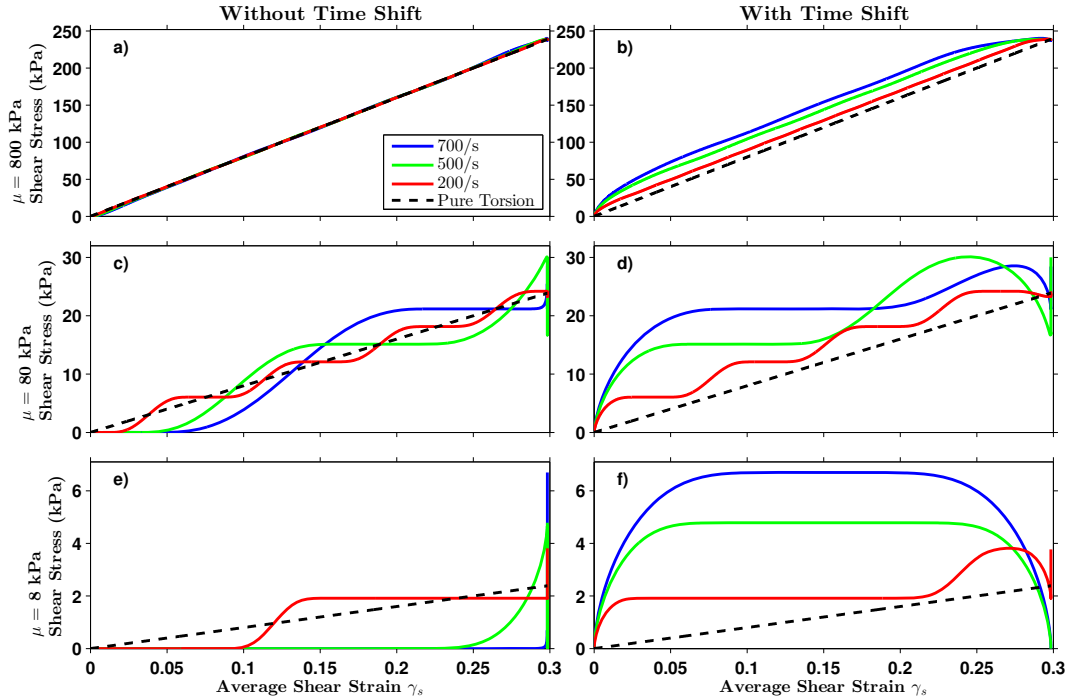
**Figure 4.** Panel pairs *a–b*, *c–d*, and *e–f* show apparent "strain-rate effects" in three linear elastic materials with shear moduli $\mu = 800$, 80, and 8 kPa, respectively. Note the differences in the vertical scales for the three groups of panels. Solid colored curves are shear stress measured at the *Load Cell* plotted against the average shear strain $\gamma_s$. The black dashed lines correspond to the stress-strain curve that results for a pure torsional deformation in dynamic equilibrium.

of 0.3 by 679 μs (the pulse duration). For $t > t_{\text{travel}} = 601$ μs, the strain at the *Load Cell* increases to roughly 0.8 (see panel *h* in Figure 3) and subsequently falls to zero strain, and of course, the stress at the *Load Cell* is proportional to this strain. Thus, a parametric plot of $\sigma_{\text{Load Cell}}(t)$ versus $\gamma_s(t)$ becomes essentially a vertical line at $\gamma_s = 0.3$, where a single average shear strain maps to infinitely many stresses.

When the $\mu = 80$ and 8 kPa data is plotted with a time shift (panels *d* and *f* in Figure 4), the data *appears* more reasonable but is still completely erroneous. In particular, the "initial" shear moduli (that is, the slopes of the stress-strain curves at the origin) are substantially higher than the actual shear modulus of the linear elastic specimen, which is the slope of the dashed curve. For strains up to 0.05, our 700/s curves (for $\mu = 8$ and 80 kPa) agree qualitatively, though not quantitatively,[14] with the 700/s stress-strain curves for bovine brain tissue in Figures 5 and 6 of [Nie et al. 2013]. In particular, their stress-strain curves have no initially flat region of the type in panels *c* and *e* in our Figure 4. Based on these observations, it would appear that Nie et al. [2013] time-shifted the *Load Cell* data to synchronize it with the average strain data in order to generate the stress-strain curves for the "700/s" tests that they reported. But regardless

---

[14] Our linear elastic simulations for $\dot{\gamma}_{\text{max}} = 700$/s were not intended or expected to *fit* the 700/s stress-strain curves in [Nie et al. 2013]. Their quasistatic curves show large nonlinear elastic effects that would be expected to persist in dynamic tests.

of whether they time-shifted their *Load Cell* data, the results in this section indicate that the stress-strain curves reported for bovine brain tissue in [Nie et al. 2013] most likely have large systematic errors in the strains. The results in the next paragraph lend further support for this conclusion.

The 700/s curve in Figure 6 of [Nie et al. 2013] is an average of the 700/s stress-strain curves for their five samples. From this curve, they estimated an (average) initial shear modulus of 53.5 kPa. If this were an accurate estimate of the instantaneous elastic shear modulus of a *viscoelastic* specimen, then the shear wave speed in the specimen would be controlled by this modulus, giving a travel time in the specimen of 232 $\mu$s. Our $\mu = 80$ kPa elastic simulations are closest to this case with an even shorter travel time of 190 $\mu$s. However, as panels $c$ and $d$ in Figure 4 and panels $e$ and $f$ in Figure 3 show, dynamic equilibrium is not reached even for this stiffer case.

It is clear that the apparent "rate effects" discussed here are not due to viscoelastic or viscoplastic behavior in the specimen. Rather, they are due to the fact that the average shear strain, which is used to construct the stress-strain curves, is significantly different from the strain at the location where the stress is measured. However, in a Kolsky bar test on specimens that exhibit rate-dependent behavior, the distinction between the actual material response and apparent "rate effects" would be lost. Thus, one might falsely attribute the apparent rate effects discussed above to either viscoelastic or viscoplastic properties of the specimen.

After this portion of the paper had been completed, private communications with Xu Nie (the first author of [Nie et al. 2013]) suggested some possibilities that were not considered above. Nie stated that in generating their stress-strain curves, they did not time-shift the *Load Cell* data to synchronize it with the average strain data.[15] Furthermore, he estimated that the travel time in the specimen was approximately 30 $\mu$s. This estimate was obtained from the difference between the arrival time of the loading wave at the specimen and the onset of a signal at the *Load Cell*. These times were estimated from oscilloscope traces from one test.[16] Clearly, a travel time of 30 $\mu$s is inconsistent with the results presented here for a specimen as soft as brain tissue. Indeed, it would imply an instantaneous elastic shear modulus of 3.2 MPa, which is totally unreasonable for brain tissue.

On examining a snapshot of the oscilloscope traces provided to us by Xu Nie, we noticed that there was a discontinuity in the slope of the *Load Cell* signal at about 260 $\mu$s.[17] Subsequently, the *Load Cell* signal exhibits a substantial increase in noise. We suspect that the travel time of the *torsional shear wave* in the specimen was (approximately) 260 $\mu$s and that the onset of the *Load Cell* signal at 30 $\mu$s is due to some other source. Note that a travel time of 260 $\mu$s would imply an instantaneous elastic shear modulus of 42 kPa, which is not unreasonable. The early *Load Cell* signal would also explain why the stress-strain curves in [Nie et al. 2013] do not exhibit an initially flat region even though they claim that the data was plotted without a time shift. Indeed, no such region is observable in panel $a$ of Figure 4 even though the travel time in that case was 60 $\mu$s. If our conjecture is correct, then the shear stress inferred from the

---

[15] They did, of course, perform the necessary time shift of the strain gage data to account for the time it takes the shear wave to propagate from the strain gage to the specimen end of the incident bar.

[16] Nie points out (and we agree) that such estimates for arrival and onset times, and particularly for their differences, are subject to errors that are difficult to bound. Our estimate of the actual travel time of the shear wave, and consequently our estimate for the instantaneous elastic shear modulus for the specimen, are subject to even more uncertainty. However, it is only the order of magnitude of these estimates that are essential for the arguments given here.

[17] To simplify the discussion, we take the arrival time of the loading wave at the specimen to be $t = 0$ as has been assumed previously this paper.

*Load Cell* signal would be erroneous from 30–260 $\mu$s (and hence for the smaller strains), and possibly for later times as well, depending on how long this spurious signal persisted.

A possible explanation for the early onset of the *Load Cell* signal is the presence of bending or longitudinal waves in the incident bar, which would travel faster than the torsional shear wave. Another possible explanation is the longitudinal precursor wave that is generated in the specimen by the shearing deformation from the torsional wave. This precursor wave is a real effect as discussed in the analysis of our three-dimensional dynamic simulations in Section 5. But it is not clear to us whether any of these waves could even generate a measurable signal in the *torque* sensor, so at the moment, the early onset of this signal remains unresolved.

**3E.** *Increasing the quality of the test.* In the previous sections, we examined the axially nonuniform strain and strain-rate states that may exist in the specimen in torsional Kolsky bar tests. For sufficiently soft specimens, large systematic error in the stress-strain curves is associated with the loading conditions and the specimen lengths considered. In this section, we discuss some alterations to the experiment that might alleviate this error. Some dimensional analysis is particularly useful here and can indicate how to improve the experimental setup.

Using parameters specific to our loading pulse, by (2-7) and (2-8), we see that the total average strain and the pulse duration can be expressed as

$$\gamma_{\max} = (t_r + t_p)\dot{\gamma}_{\max}, \qquad t_d = 2t_r + t_p = t_r + \frac{\gamma_{\max}}{\dot{\gamma}_{\max}} = 2\frac{\gamma_{\max}}{\dot{\gamma}_{\max}} - t_p. \tag{3-19}$$

If we take $\dot{\gamma}_{\max}$ as fixed, we need only specify two of the three parameters $t_r$, $t_p$, and $\gamma_{\max}$ in order to determine the four parameters $t_r$, $t_p$, $\gamma_{\max}$, and $t_d$. We choose to track changes by altering the rise time $t_r$ and the plateau duration $t_p$.

Two quality measures of the test conditions are the ratio $Q_r$ of the rise time to the travel time and the ratio $Q_p$ of the plateau time to the travel time:

$$Q_r \equiv \frac{t_r}{t_{\text{travel}}} = \frac{ct_r}{L} = \frac{t_r}{L}\sqrt{\frac{\mu}{\rho}}, \qquad Q_p \equiv \frac{t_p}{t_{\text{travel}}} = \frac{ct_p}{L} = \frac{t_p}{L}\sqrt{\frac{\mu}{\rho}}. \tag{3-20}$$

$Q_r$ can be thought of as the number of wave reflections that occur during the initial rise time, and $Q_p$ can be thought of as the number of reflections that occur during the plateau period. A high quality test would be one for which both $Q_r \gg 1$ and $Q_p \gg 1$. We emphasize that these measures are dimensionless and depend on the details of the loading pulse, the specimen length, and the shear wave speed of the specimen.

For a given range of values of the shear wave speed $c$, the parameters $L$, $t_d$, $t_r$, $t_p$, $\gamma_{\max}$, or $\dot{\gamma}_{\max}$ can be chosen to ensure a large quality factor. The $\mu = 800$ kPa case in Figure 4 (panel *a*) gave the most accurate results; here $Q_r = 4.2$ for all three cases, and $Q_p = 2.98$, $5.82$, and $20.8$ for $\dot{\gamma}_{\max} = 700$/s, $500$/s, and $200$/s, respectively. For our particular examples, transitioning from $\mu = 800$ kPa to $\mu = 8$ kPa reduces the wave speed by a factor of ten. This also reduces $Q$ by a factor of ten.[18] Thus, to perform a valid experiment, the parameters that determine $Q$ need to be adjusted in the softer material case to compensate for the slower wave speed and thus restore $Q$ to a larger value.

An obvious change to make is reducing the specimen length. Although in practice this might be quite difficult for brain tissue, reducing the length (i.e., thickness) of the specimen by a factor of 10 (from 1.7

---

[18]The symbol $Q$ without an $r$ or $p$ subscript refers to *both* $Q_r$ and $Q_p$.

to 0.17 mm) would increase $Q$ by a factor of 10. However, by reducing the length, inhomogeneities in the tissue are more likely to influence measurements. There are also practical concerns: how to cut slices that are submillimeter, how to handle them, and the effects of gluing them.

Another means of increasing the quality $Q_r$ is to increase the rise time of the loading pulse. To increase $Q_r$ by a factor of 10 without reducing the specimen length, $t_r$ must also increase by a factor of 10; i.e., we need $t_r = 2500\,\mu s$. From $(3\text{-}19)_1$, we see that this can be achieved by reducing the maximum (average) strain-rate $\dot{\gamma}_{\max}$ or by increasing the maximum (average) strain $\gamma_{\max}$. However, in an actual torsion test, buckling or tearing is likely to occur at sufficiently large strain. Similar comments apply to $Q_p$ and $t_p$.

There are experimental constraints on the duration of the loading pulse, namely the bar length, bar wave speed, and location of the strain gage on the bar. Attempting to accommodate a long (e.g., 7 ms) loading pulse for an aluminum or steel bar by only increasing its length would yield impractical bar lengths. However, a considerable increase in loading pulse duration can be gained by switching to polymer bars without changing the length of the bar. For example, polycarbonate (PC) and polymethyl methacrylate (PMMA) have shear wave speeds of 0.91 mm/$\mu$s and 1.3 mm/$\mu$s, respectively. Compared to aluminum or steel bars, which have shear wave speeds on the order of 3 mm/$\mu$s, the longest pulse for a fixed length of bar would be increased by 3.6 and 2.5 for a PC and a PMMA bar, respectively.

Additional gains can be made in accommodating longer loading pulses by replacing the strain gage with an optical measurement of the angle of twist imposed on the specimen. The traditional analysis of Kolsky bar test data uses the fact that the average strain-rate in the specimen is proportional to the strain generated in the incident bar by the reflected wave, *assuming the specimen is in dynamic equilibrium*; see (7) in [Gilat 2000] for torsion tests and [Gray 2000; Chen and Song 2011] for compression tests. For sufficiently long loading pulses, however, the incident and reflected waves can overlap at the strain gage location, in which case the reflected wave signal cannot be separated from the combined signal, making it impossible to extract the strain in the incident bar associated with the reflected wave.[19] This would no longer be an issue with an optical measurement of the angle of twist at the end of the incident bar adjacent to the specimen. Also, since the specimens could not have been in dynamic equilibrium in the tests of [Nie et al. 2013], the method discussed above for determining the strain-rate in the specimen can be called into question. This issue would also be bypassed by direct optical measurement of the angle of twist.

**3F.** *A parametric study of test quality.*  In view of the discussion in the previous section, we conducted a parametric study in which $t_r$ and $t_p$ were varied in an attempt to increase the quality of the test within the experimental constraints. For these simulations, we used $\dot{\gamma}_{\max} = 700/s$, $\mu = 8\,\mathrm{kPa}$, and $L = 1.7\,\mathrm{mm}$. With these parameters fixed, and varying only the rise time and plateau time, we present in Figure 5 the results on the peak strain reached at the *Load Cell* during the simulation (panel *a*), the total duration of the loading pulse (panel *b*), and the average error (panel *c*) as defined below.

Equation (3-19) predicts that, for a fixed maximum average strain-rate $\dot{\gamma}_{\max}$, the maximum *average* strain $\gamma_{\max}$ depends linearly on the sum of $t_r$ and $t_p$. In panel *a*, the *actual peak strain* in the specimen at the *Load Cell*, $\max[\gamma]$, i.e., the maximum value of $\gamma(L, t)$ over the duration of the experiment, deviates

---

[19] This was one of the difficulties encountered by Nie et al. [2013]. They partially bypassed the problem by substituting the (negative of the) incident wave for the reflected wave, arguing that this is a good approximation for very soft specimens, which in fact it may be. They could then use the measured strain in the incident bar due to the incident wave at least up until the time of arrival of the reflected wave.
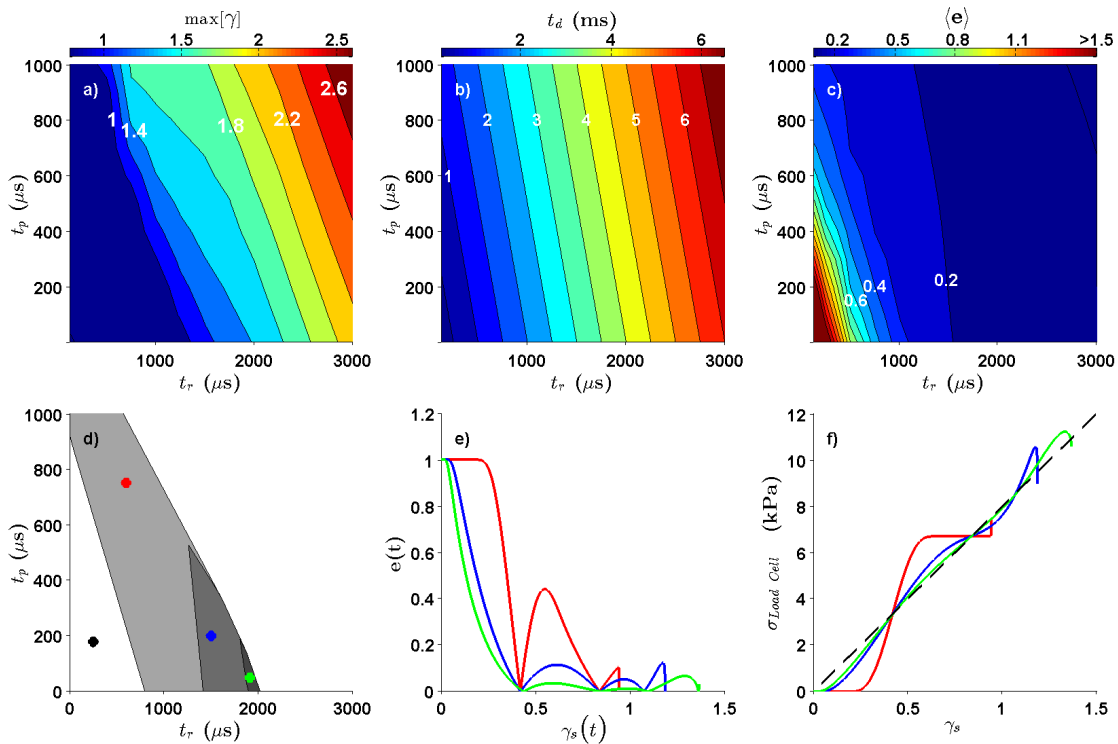
**Figure 5.** Panels *a–c* show the effects of varying the rise time $t_r$ (horizontal axis) and the plateau time $t_p$ (vertical axis) for $\dot{\gamma}_{max} = 700/s$ tests on a linear elastic specimen with shear modulus 8 kPa. Through false-color images, these panels show the peak strain reached at the *Load Cell* during a simulation ($\max[\gamma]$, panel *a*), the total loading pulse duration $t_d$ (panel *b*), and the average error $\langle e \rangle$ in the strain (see text, panel *c*). Panel *d* shows the regions where the peak strain is less than 1.5, the total pulse duration less than 5 ms, and the average error less than 40%, 20%, and 15% in darkening shades of gray. The black dot represents *Simulation III*, which most closely resembles the test conditions in [Nie et al. 2013]. The red, blue, and green circles are sample test conditions taken in each region. Additional results for these test conditions are given in panels *e* and *f*. Panel *e* is a plot of *e*(*t*) (the relative error in the strain at the *Load Cell*) versus the average imposed strain $\gamma_s(t)$. Panel *f* shows the resultant stress-strain curves. The black dashed line represents the ideal to which these curves should be compared, that is, the curve that would have been produced if $\gamma_s(t)$ coincided with $\gamma_{\text{Load Cell}}$.

from this simple behavior. This is most clearly seen for the smaller values of $t_r$ and $t_p$. For example, when $t_r = 250\,\mu s$ and $t_p = 179\,\mu s$, the maximum average strain $\gamma_{max} = 0.3$, but the peak strain is close to 1 (*Simulation III*). These larger strains, as discussed in the previous section, are from a failure to achieve dynamic equilibrium.

Panel *b* shows the dependence of the pulse duration $t_d$ on the rise time and plateau time, also given by (3-19). This panel is relevant to the constraints introduced from the lengths of the bars in a Kolsky bar experiment. As discussed earlier, a 7 ms long pulse may be unmanageable in an aluminum or steel bar.

Since there are nonuniform strains experienced in the specimen, there is an error associated with assuming that the measured average shear strain $\gamma_s(t)$ is equal to the shear strain at the *Load Cell*, $\gamma(L, t)$. We therefore take the relative error in the strain measurement at time $t$ to be

$$e(t) = \frac{|\gamma(L, t) - \gamma_s(t)|}{\gamma_s(t)}. \tag{3-21}$$

This error is time-dependent and is small when near-uniform conditions exist within the specimen. Since $\gamma(L, t) = 0$ prior to the arrival of the shear wave at the *Load Cell*, the value of the error $e(t)$ in (3-21) is 1 for all times less than the travel time. We ignore the error during these early times since we hold the travel time fixed in this section. We define an average error by using the time average of its value starting after the travel time until a later time $t_{\max}$

$$\langle e \rangle = \frac{1}{t_{\max} - t_{\text{travel}}} \int_{t_{\text{travel}}}^{t_{\max}} e(t) \, dt. \tag{3-22}$$

Qualitatively similar results were found for various values of $t_{\max}$, and in what follows, we chose a large integration window where $t_{\max} = 15\,\text{ms}$ (roughly twice the value of the longest pulse duration considered). Thus, the average error is an estimate of the sensitivity of a torsion test to the parameters of the loading pulse.

Panel $c$ in Figure 5 presents the dependence of the average error $\langle e \rangle$ on the rise time and plateau time. This panel clearly shows that error is reduced by increasing both the rise time and the plateau time as suggested by (3-20) although it depends most critically on the rise time. For sufficiently large rise times, the effects of the plateau time become negligible.

Combining the limitations introduced by the specimen in terms of maximum allowable strain, the constraint from bar lengths in terms of total duration of the pulse, and the acceptable error in the measurement, we can determine whether it is possible to design an experiment that reaches dynamic equilibrium for a given imposed average strain-rate. The small dark gray region in panel $d$ in Figure 5 (small triangular region near $t_r = 2000\,\mu\text{s}$) represents the rise and plateau times where the peak strain at the *Load Cell* is less than 1.5, the loading pulse duration is less than 5 ms, and the average error is less than 15%. The two neighboring lighter shades of gray correspond to the regions where rise and plateau times satisfy the same requirements in peak strain and loading pulse duration but relax the average error constraint to 20 and 40%. Although not clear in the presentation of the colored regions, these regions overlap so that the light gray region extends "underneath" the two darker shades of gray, and the medium gray region extends under the dark gray region (but not under the light gray). An average strain of 1.5 corresponds to roughly a 17° rotation of one end of the specimen with dimensions given in Table 2. Achieving a pulse that is 5 ms long would require a *polymer bar* approximately 5 m long, depending on how the strain was measured. The error bounds were taken fairly loosely since actual error is time-dependent and therefore depends on the average imposed strain $\gamma_s$. The red, green, and blue circles in panel $d$ are three sample test conditions, one taken in each region of error. The black dot outside the gray regions represents *Simulation III*, which most closely resembles the test conditions in [Nie et al. 2013].

Panel $e$ in Figure 5 is the error $e(t)$ plotted against the imposed average strain $\gamma_s(t)$ for the three sample test conditions discussed above. This panel shows that, even for the most accurate test (green line), the initial ring-up period extends until moderate strains of about 0.4 are reached. This means that even in

these experiments the small and moderate strain region of the stress-strain curve would be unreliable. Panel $f$ shows the resultant stress-strain curves from each of the color-coded simulations. Here, as in Figure 4, the black dashed line represents the ideal to which these curves should be compared, that is, the curve that would have been produced if $\gamma_s(t)$ coincided with $\gamma_{\text{Load Cell}}$. Long loading pulses[20] and large strains are necessary to reproduce the linear stress-strain curve in the most accurate test (green line).

## 4. Quasistatic torsion of isotropic nonlinear elastic specimens[21]

In this section, we examine the stress state in isotropic nonlinear elastic materials undergoing various types of quasistatic torsional deformation. The general constitutive relation for incompressible isotropic elastic solids is discussed in Section 4A. The strain state in pure torsion is considered in Section 4B. The stress state for pure torsion of a general incompressible isotropic elastic solid is derived in Section 4C, and the stress state for the special case of a Mooney–Rivlin material is considered in Section 4D. The specimens in Sections 4B–4D may be either annular or disc-shaped. For incompressible annular specimens, radially nonuniform torsional deformations are briefly discussed in Section 4E; such deformations are necessary in order to satisfy the stress-free boundary condition on both the outer and inner surfaces.

In Section 4F, we present the results of our three-dimensional quasistatic torsion simulations for short, nearly incompressible, annular specimens with glued ends and stress-free inner and outer surfaces. The constitutive model used in these simulations is a compressible version of the Mooney–Rivlin model. The boundary conditions in these simulations, which mimic those in the tests by Nie et al. [2013], do not allow the annular specimens to undergo pure torsion or the radially nonuniform torsion considered in Section 4E. The stress components obtained in the simulations are compared with the analytical results for pure torsion from Sections 4C and 4D.

**4A.** *Incompressible isotropic nonlinear elastic solids.* The Cauchy stress tensor $T$ can be decomposed into a pressure (or hydrostatic stress) $p$ and a deviatoric stress tensor $S$ (i.e., $\operatorname{tr} S = 0$):

$$T = -pI + S, \qquad p \equiv -\tfrac{1}{3}\operatorname{tr} T, \qquad S = \operatorname{dev} T \equiv T - \tfrac{1}{3}(\operatorname{tr} T)I. \tag{4-1}$$

Here $I$ denotes the identity tensor. The standard sign convention for the Cauchy stress tensor is used in this paper: normal stress components are taken positive in tension. However, the pressure $p$ is positive in compression. It is sometimes simpler to decompose $T$ as

$$T = -\hat{p}I + \hat{S}, \tag{4-2}$$

where the tensor $\hat{S}$ need not be deviatoric, in which case the scalar $\hat{p}$ need not equal the pressure $p$.[22] Consistency with the relations (4-1) requires that

$$p = \hat{p} - \tfrac{1}{3}\operatorname{tr} \hat{S}, \qquad S = \operatorname{dev} \hat{S}. \tag{4-3}$$

---

[20]In this case, the notion of "constant strain-rate" should be modified to "peak strain-rate" since the plateau time is small compared to the rise time.

[21]General background for some of the material in Sections 4A–4E can be found in the books [Green and Adkins 1960; Truesdell and Noll 1965; Treloar 1975; Batra 2006] and the papers [Rivlin 1948b; 1949; Beatty 1987].

[22] Nevertheless, some authors still refer to $\hat{p}$ as "the pressure" in this case.

For a compressible (i.e., unconstrained) material, a constitutive relation must be provided for $\boldsymbol{T}$ and, equivalently, for $p$ and $\boldsymbol{S}$ or for $\hat{p}$ and $\hat{\boldsymbol{S}}$.

For an incompressible material, $p$ and $\hat{p}$ are indeterminate in the sense that they are not subject to any constitutive relation. However, their values at each point in the material must be such that the boundary conditions and momentum balance equations (or, in the quasistatic case, the equilibrium equations) are satisfied. For an incompressible material, a constitutive relation need only be provided for $\boldsymbol{S}$ or $\hat{\boldsymbol{S}}$, which are referred to as the determinate parts of the stress.

For an incompressible elastic material, the determinate stress $\hat{\boldsymbol{S}}$ is, by definition, a function of the deformation gradient $\boldsymbol{F}$. If the material is also isotropic, then $\hat{\boldsymbol{S}}$ is an isotropic function of the left Cauchy–Green deformation tensor $\boldsymbol{B} = \boldsymbol{F}\boldsymbol{F}^T$. A general representation for such functions is given by

$$\hat{\boldsymbol{S}} = \mu\left[\omega\boldsymbol{B} - (1-\omega)\boldsymbol{B}^{-1}\right] = 2C_1\boldsymbol{B} - 2C_2\boldsymbol{B}^{-1}, \tag{4-4}$$

where

$$C_1 = \tfrac{1}{2}\mu\omega, \qquad C_2 = \tfrac{1}{2}\mu(1-\omega), \qquad \mu = 2(C_1 + C_2), \qquad \omega = \frac{C_1}{C_1 + C_2}. \tag{4-5}$$

The elastic moduli $C_1$, $C_2$, and $\mu$ and the dimensionless parameter $\omega$ are scalar-valued functions of $\operatorname{tr}\boldsymbol{B}$ and $\operatorname{tr}\boldsymbol{B}^{-1}$. In particular, $\mu = \tilde{\mu}(\operatorname{tr}\boldsymbol{B}, \operatorname{tr}\boldsymbol{B}^{-1})$ can be interpreted as a (generally strain-dependent) shear modulus.[23] For infinitesimal deformations, the deviatoric part of the constitutive relation (4-4) reduces to the linear elastic constitutive relation for the deviatoric stress tensor: $\boldsymbol{S} = 2\mu_0 \operatorname{dev}\boldsymbol{\epsilon}$, where $\boldsymbol{\epsilon}$ is the infinitesimal strain tensor and $\mu_0 = \tilde{\mu}(3, 3)$ since $\operatorname{tr}\boldsymbol{B} = \operatorname{tr}\boldsymbol{B}^{-1} = \operatorname{tr}\boldsymbol{I} = 3$ in the undeformed state. Thus, $\mu_0$ is the linear elastic shear modulus that was denoted by $\mu$ in previous sections.

Specification of either set of constitutive functions $\mu, \omega$ or $C_1, C_2$ determines a particular material within the general class of incompressible isotropic elastic materials. At this point, we do not assume that the material is hyperelastic since this condition is not necessary for any of the results on the stress state in pure torsion in Section 4C.[24] However, the incompressible Mooney–Rivlin model considered in Section 4D and the compressible version of this model used in the three-dimensional simulations (Sections 4F and 5A) are hyperelastic.

It has been found that the inequalities $C_1 > 0$ and $C_2 \geq 0$ imply physically reasonable response and are consistent with experimental data on many nearly incompressible isotropic elastic solids.[25] These inequalities, which are equivalent to

$$\mu > 0, \qquad 0 < \omega \leq 1, \tag{4-6}$$

are assumed throughout this paper. Then $0 \leq 1 - \omega < 1$ also.

---

[23] See also (4-16) below for the case of pure torsional deformations.

[24] If the material is hyperelastic, then the stress tensor is derivable from a strain energy (per unit volume) $W$ with $W = \widetilde{W}(\operatorname{tr}\boldsymbol{B}, \operatorname{tr}\boldsymbol{B}^{-1})$ for an incompressible isotropic elastic material. Consequently, the coefficient functions $\mu, \omega$ and $C_1, C_2$ in (4-4) are determined by $W$; e.g., $C_1 = \partial W/\partial(\operatorname{tr}\boldsymbol{B})$ and $C_2 = \partial W/\partial(\operatorname{tr}\boldsymbol{B}^{-1})$. It follows that $C_1$ and $C_2$ are not independent although neither function completely determines the other. Similar comments apply to $\mu$ and $\omega$ although their expressions in terms of the derivatives of $W$ are more complicated.

[25] See [Truesdell and Noll 1965, §49, §53] and [Beatty 1987], where these are referred to as the E-inequalities.

**4B.** *Pure torsional deformation.* A *pure torsional deformation* satisfying the boundary conditions (2-2) is given by (3-1) with the angular displacement $\delta$ as in (3-13):

$$r = R, \qquad \theta = \hat{\theta}(\Theta, Z) = \Theta + \psi(Z - L), \qquad z = Z. \qquad (4\text{-}7)$$

We assume that the angle of twist per unit length, $\psi$, is positive: $\psi > 0$. For this deformation, the physical components[26] of the deformation gradient $\boldsymbol{F}$, the left Cauchy–Green tensor $\boldsymbol{B} \equiv \boldsymbol{F}\boldsymbol{F}^T$, and its inverse $\boldsymbol{B}^{-1}$ are given by

$$[\boldsymbol{F}] = \begin{bmatrix} 1 & 0 & 0 \\ 0 & 1 & \psi r \\ 0 & 0 & 1 \end{bmatrix}, \qquad [\boldsymbol{B}] = \begin{bmatrix} 1 & 0 & 0 \\ 0 & 1+\psi^2 r^2 & \psi r \\ 0 & \psi r & 1 \end{bmatrix}, \qquad [\boldsymbol{B}^{-1}] = \begin{bmatrix} 1 & 0 & 0 \\ 0 & 1 & -\psi r \\ 0 & -\psi r & 1+\psi^2 r^2 \end{bmatrix}. \qquad (4\text{-}8)$$

Thus, pure torsion is radially inhomogeneous and isochoric ($\det \boldsymbol{F} = 1$). The Eulerian finite strain tensors corresponding to $\boldsymbol{B}$ and $\boldsymbol{B}^{-1}$ are $\boldsymbol{E} = \frac{1}{2}(\boldsymbol{B} - \boldsymbol{I})$ and $\boldsymbol{\mathcal{E}} = \frac{1}{2}(\boldsymbol{I} - \boldsymbol{B}^{-1})$; the latter is known as the Almansi strain tensor. For pure torsion, the only nonzero components of $\boldsymbol{E}$ and $\boldsymbol{\mathcal{E}}$ are $E_{\theta\theta} = \psi^2 r^2$, $\mathcal{E}_{zz} = -\psi^2 r^2$, and

$$E_{\theta z} = E_{z\theta} = \mathcal{E}_{\theta z} = \mathcal{E}_{z\theta} = \tfrac{1}{2}\psi r, \qquad (4\text{-}9)$$

which is a measure of the shear strain in pure torsion.[27]

The volume average of the shear strain $E_{\theta z}$ is given by

$$\langle E_{\theta z}\rangle \equiv \frac{1}{V}\iiint E_{\theta z}\, \mathrm{d}V = \tfrac{1}{3}\psi\,\frac{R_o^2 + R_i R_o + R_i^2}{R_i + R_o}. \qquad (4\text{-}10)$$

Since $E_{\theta z}$ is independent of $z$, this is also the average over the annular cross-section at any given axial location. $\langle E_{\theta z}\rangle$ can also be expressed in terms of the average radius $\bar{R}$ and the radial difference $\Delta$ (see (2-1)):

$$\langle E_{\theta z}\rangle = \tfrac{1}{3}\psi\,\frac{(3\bar{R}^2 + \Delta^2)}{2\bar{R}} = \tfrac{1}{2}\psi\bar{R}\left[1 + \tfrac{1}{3}\left(\frac{\Delta}{\bar{R}}\right)^2\right] \approx \tfrac{1}{2}\psi\bar{R}, \qquad (4\text{-}11)$$

where the approximation is valid when $\Delta/\bar{R} \ll 1$. The relative error in approximating $E_{\theta z}$ by $\frac{1}{2}\psi\bar{R}$ takes on all values between the following bounds:

$$\frac{-\Delta/\bar{R}}{1-\Delta/\bar{R}} \leq \frac{E_{\theta z} - \tfrac{1}{2}\psi\bar{R}}{E_{\theta z}} \leq \frac{\Delta/\bar{R}}{1+\Delta/\bar{R}}. \qquad (4\text{-}12)$$

The relative error of largest absolute value occurs at the inner surface and is given by the absolute value of the expression on the left. For the specimen dimensions considered here (see Table 1), the largest relative error in approximating $E_{\theta z}$ by its average is 15%.

As discussed in Section 2B, for torsion tests, a measure of average shear strain often used in the experimental literature is $\gamma_s$ as defined in (2-5), that is, $\gamma_s = \psi\bar{R}$. By (4-11), it follows that

$$\gamma_s \approx 2\langle E_{\theta z}\rangle \qquad (4\text{-}13)$$

---

[26] Recall that these are the components relative to the unit basis vectors along the cylindrical coordinate directions.

[27] In general, both $\boldsymbol{E}$ and $\boldsymbol{\mathcal{E}}$ reduce to the infinitesimal strain tensor $\boldsymbol{\epsilon}$ in the limit of small displacement gradients. This fact, together with (4-9), yields $\epsilon_{\theta z} = \frac{1}{2}\psi r$ for infinitesimal deformations, consistent with (3-14).

with the relative error in this approximation being given by

$$\frac{2\langle E_{\theta z}\rangle - \gamma_s}{\gamma_s} = \tfrac{1}{3}\left(\frac{\Delta}{\bar{R}}\right)^2. \tag{4-14}$$

For the specimen dimensions in Table 1, this is about 0.0056, that is, a relative error of about 0.56%.

Finally, note that, while annular specimens have been assumed in part of the discussion above, most of the results in this section are also valid for disc-shaped specimens ($R_i = 0$). The approximation on the right side of (4-11) is no longer valid in this case since $\Delta/\bar{R} = 1$. Also, the lower bound in (4-12) becomes $-\infty$ since $\Delta/\bar{R} \to 1$ from below as $R_i \to 0$. This latter result also follows from the fact that $E_{\theta z} = 0$ at $r = 0$ whereas $\tfrac{1}{2}\psi\bar{R} > 0$.

**4C.** *Stress state in pure torsion of incompressible isotropic elastic specimens.* In this and the next section, we discuss the stress state in pure torsion of an incompressible, isotropic, nonlinear elastic solid. The results in these sections are valid for both annular and disc-shaped specimens. In this section, we consider the general constitutive relation (4-4)$_1$ for the determinate stress $\hat{S}$ subject only to the inequalities (4-6) for the coefficient functions $\mu$ and $\omega$. In the next section, we consider the special case where these functions are taken to be constants. Recall that $\mu$ and $\omega$ are generally scalar-valued functions of tr $B$ and tr $B^{-1}$. Since tr $B =$ tr $B^{-1} = 3 + \psi^2 r^2$ for pure torsion, we have

$$\mu = \tilde{\mu}(\text{tr } B, \text{tr } B^{-1}) = \tilde{\mu}(3 + \psi^2 r^2, 3 + \psi^2 r^2) \equiv \hat{\mu}(\psi^2 r^2) \tag{4-15}$$

in this case and similarly for $\omega$, $C_1$, and $C_2$.

For pure torsion, the shear stress components are given by [Rivlin 1947; 1948b; 1949]

$$T_{\theta z} = \mu\psi r = 2\mu E_{\theta z}, \qquad T_{rz} = T_{r\theta} = 0, \tag{4-16}$$

and the differences in the normal stress components are given by

$$T_{\theta\theta} - T_{zz} = \mu\psi^2 r^2, \qquad T_{\theta\theta} - T_{rr} = \mu\omega\psi^2 r^2, \qquad T_{rr} - T_{zz} = \mu(1-\omega)\psi^2 r^2. \tag{4-17}$$

These relations follow from (4-2), (4-4)$_1$, and (4-8). It is clear that the stress state is radially inhomogeneous. We refer to the shear stress component $T_{\theta z}$ as the *torsional stress*. From (4-16), we see that $\mu$ can be interpreted as a shear modulus and that $T_{\theta z} > 0$ (since we assume $\psi > 0$) with the exception that $T_{\theta z} = 0$ at $r = 0$ for a disc-shaped specimen.

From the relations in (4-16) and (4-17), we see that the normal stress differences are proportional to the torsional stress:

$$T_{\theta\theta} - T_{zz} = \psi r \cdot T_{\theta z}, \qquad T_{\theta\theta} - T_{rr} = \omega\psi r \cdot T_{\theta z}, \qquad T_{rr} - T_{zz} = (1-\omega)\psi r \cdot T_{\theta z}. \tag{4-18}$$

The relation on the left in (4-18) is a *universal relation* between the hoop, axial, and torsional stress: it does not explicitly involve the constitutive functions $\mu$ or $\omega$ in the representation (4-4)$_1$ for the determinate stress.

To determine the normal stress components (as opposed to just their differences), we need to utilize the equilibrium equations and boundary conditions. Since $T_{r\theta}$ and $T_{rz}$ are zero throughout the specimen, the radial component of the equilibrium equation reduces to

$$\frac{\partial T_{rr}}{\partial r} + \frac{T_{rr} - T_{\theta\theta}}{r} = 0, \tag{4-19}$$

and the assumption that the outer lateral surface ($r = R_o$) is stress-free reduces to the requirement that $T_{rr} = 0$ at $r = R_o$. On using $(4\text{-}17)_2$ to evaluate the $T_{rr} - T_{\theta\theta}$ term above, integrating from $r$ to $R_o$, and then using $T_{rr}|_{r=R_o} = 0$, we obtain the following relation for the radial stress:

$$T_{rr} = -\psi^2 \int_r^{R_o} \mu\omega r \, \mathrm{d}r = -2\psi^2 \int_r^{R_o} C_1 r \, \mathrm{d}r. \tag{4-20}$$

Then from (4-17), we see that the hoop and axial stresses are given by

$$T_{\theta\theta} = T_{rr} + \mu\omega\psi^2 r^2, \qquad T_{zz} = T_{rr} - \mu(1-\omega)\psi^2 r^2 \tag{4-21}$$

with $T_{rr}$ as in (4-20). Since $\mu$ and $\omega$ are functions of $\psi^2 r^2$, it follows that $T_{rr}$, $T_{\theta\theta}$, $T_{zz}$, and $T_{\theta z}$ depend only on $\psi$ and $r$ while $T_{r\theta} = T_{rz} = 0$. These results imply that all terms in the $\theta$ and $z$ components of the equilibrium equation are identically zero. Thus, pure torsion is possible in any incompressible, isotropic, nonlinear elastic specimen (disc-shaped or annular), and the outer surface $R = R_o$ may be taken to be stress-free [Rivlin 1947; 1948b; 1949].[28]

Since $\mu$, $\omega$ and $C_1$ are functions of $\psi^2 r^2$, the integral for $T_{rr}$ cannot be evaluated unless $C_1$ (equivalently, the product $\mu\omega$) is specified. However, since $\mu$ and $\omega$ are positive and $\omega \leq 1$ and $\psi \neq 0$,[29] important qualitative properties of the normal stress components may be inferred directly from (4-20) and (4-21), as summarized below.[30]

For pure torsion of an incompressible, isotropic, nonlinear elastic specimen (disc-shaped or annular) with stress-free outer surface $r = R_o$, we have:

**Conclusion 1.** $T_{rr}$ is negative for $R_i \leq r < R_o$. Thus, the radial stress is compressive except at the outer surface, where it is zero. Furthermore, the magnitude of the radial stress increases with increasing radial distance from the outer surface.

**Conclusion 2.** Since $T_{rr} < 0$ at $r = R_i$, for annular specimens (where $R_i > 0$), we see that a (nonzero) compressive normal stress must be applied on the inner surface in order that radial equilibrium be satisfied. If this compressive stress is not applied, then the specimen cannot undergo a pure torsional deformation.

**Conclusion 3.** Since $T_{rr} < 0$ for $R_i \leq r < R_o$, it follows that $T_{zz} < 0$ for $R_i \leq r < R_o$ and $T_{zz} \leq 0$ at $r = R_o$ with equality holding only if $\omega = 1$ at $r = R_o$. Thus, the axial stress is compressive everywhere except possibly at the outer surface $r = R_o$, where it is either compressive or zero.

**Conclusion 4.** Since $T_{rr} = 0$ at $r = R_o$, it follows that $T_{\theta\theta}|_{r=R_o} = \mu\omega\psi^2 r^2 > 0$. Thus, the hoop stress $T_{\theta\theta}$ is positive (i.e., tensile) at the outer surface, and by continuity, $T_{\theta\theta}$ must be tensile for some radial distance into the interior of the specimen.

**Conclusion 5.** The radial, hoop, and axial stresses depend on both constitutive functions $\mu = \hat{\mu}(\psi^2 r^2)$ and $\omega = \hat{\omega}(\psi^2 r^2)$ while the torsional stress is independent of $\omega$. It follows that *no information on the dimensionless constitutive function $\omega$ can be inferred from measurements of the torsional stress $T_{\theta z}$ alone.*[31]

---

[28] Rivlin assumed that the material is hyperelastic although that assumption is not necessary for this conclusion [Truesdell and Noll 1965, §57].

[29] Actually, we have assumed that $\psi$ is positive, but the sign of $\psi$ does not affect Conclusions 1–5.

[30] Many (but not all) of these conclusions can be found in the references cited previously.

[31] This conclusion holds even if we assume (as is reasonable) that the material is hyperelastic although we omit the proof of this result.

**4D.** *Pure torsion of Mooney–Rivlin materials.* The classical Mooney–Rivlin model[32] is a special case of the general constitutive relation for an incompressible isotropic elastic solid. It is obtained by taking the coefficient functions $C_1$ and $C_2$ (equivalently, $\mu$ and $\omega$) in the expression (4-4) for the determinate stress $\hat{S}$ to be constants.[33] The special case $C_2 = 0$ (i.e., $\omega = 1$) is known as a neo-Hookean material. For infinitesimal deformations, the deviatoric part of the Mooney–Rivlin constitutive relation reduces to $S = 2\mu \operatorname{dev} \epsilon$, where $\epsilon$ is the infinitesimal strain tensor. Thus, the constant $\mu$ in the Mooney–Rivlin model agrees with the shear modulus in the linear elastic theory [Mooney 1940; Rivlin 1947].

The Mooney–Rivlin model is one of the simplest isotropic nonlinear elastic constitutive models, and yet it still exhibits features that are in qualitative agreement with experimental data on many soft, nearly incompressible materials under moderate deformations. For this model, there are explicit closed-form expressions for all stress components in pure torsion (see below). Furthermore, a compressible version of the Mooney–Rivlin model was available in the code that we intended to use for our three-dimensional torsion simulations. For these reasons, all of our quasistatic torsion simulations (Section 4F) and most of the three-dimensional dynamic simulations (Section 5A) used this compressible version of the Mooney–Rivlin model. The following analytical results for pure torsion of an incompressible Mooney–Rivlin material will be compared with the three-dimensional quasistatic torsion simulations in Section 4F.

For Mooney–Rivlin specimens, the relation (4-16) for $T_{\theta z}$ and the relations (4-17) and (4-18) for the normal stress differences do not simplify further (aside from the fact that $\mu$ and $\omega$ are now constants). However, the relations (4-20) and (4-21) for the normal stress components reduce to[34]

$$-T_{rr} = \tfrac{1}{2}\mu\psi^2 \cdot \omega(R_o^2 - r^2) = C_1\psi^2(R_o^2 - r^2), \tag{4-22a}$$

$$T_{\theta\theta} = \tfrac{1}{2}\mu\psi^2 \cdot \omega(3r^2 - R_o^2) = C_1\psi^2(3r^2 - R_o^2), \tag{4-22b}$$

$$-T_{zz} = \tfrac{1}{2}\mu\psi^2 \cdot \left[\omega R_o^2 + (2 - 3\omega)r^2\right] = \psi^2\left[(C_1 - 2C_2)(R_o^2 - r^2) + 2C_2 R_o^2\right]. \tag{4-22c}$$

Of course, all of the conclusions at the end of Section 4C apply to the special case of Mooney–Rivlin specimens. The (compressive) radial stress that must be applied to the inner surface $r = R_i$ of an annular specimen in order to maintain a pure torsional deformation is now given explicitly by

$$T_{rr}|_{r=R_i} = -\tfrac{1}{2}\mu\psi^2 \cdot \omega(R_o^2 - R_i^2) = -\psi^2 C_1(R_o^2 - R_i^2) < 0. \tag{4-23}$$

From (4-22b), it follows that $T_{\theta\theta} > 0$ (i.e., the hoop stress is tensile) for all $R_i \leq r \leq R_o$ if and only if $R_i > R_o/\sqrt{3}$. This condition on the inner and outer radii is satisfied for the specimens in our quasistatic and dynamic simulations (see Table 1). The relations (4-22), together with $p = -\tfrac{1}{3}(T_{rr} + T_{\theta\theta} + T_{zz})$, imply that the pressure is given by

$$p = \tfrac{1}{2}\mu\psi^2 \cdot \left[\omega R_o^2 + \tfrac{1}{3}(2 - 7\omega)r^2\right]. \tag{4-24}$$

Since $\mu$ is constant, from the relation (4-16) for $T_{\theta z}$, together with the expression (4-11) for $\langle E_{\theta z}\rangle$ and

---

[32] In some of the literature, this is referred to as the Mooney model [Mooney 1940; Rivlin 1947; 1948a; 1948b; 1949; Rivlin and Saunders 1951; Green and Adkins 1960; Truesdell and Noll 1965, §95; Treloar 1975; Beatty 1987; Batra 2006].

[33] Equivalently, this is the hyperelastic material with strain energy function $W = C_1(\operatorname{tr} B - 3) + C_2(\operatorname{tr} B^{-1} - 3)$.

[34] The relations (4-22c)$_2$ and (4-23)$_2$ are some of the earliest results of [Rivlin 1947; 1948a].

the fact that $\gamma_s = \psi \bar{R}$ (see (2-5)), we see that the volume-averaged torsional stress is given by

$$\langle T_{\theta z} \rangle = 2\mu \langle E_{\theta z} \rangle = \mu \psi \bar{R} \left[ 1 + \tfrac{1}{3} \left( \frac{\Delta}{\bar{R}} \right)^2 \right] = \mu \gamma_s \left[ 1 + \tfrac{1}{3} \left( \frac{\Delta}{\bar{R}} \right)^2 \right]. \tag{4-25}$$

For the specimen dimensions in Table 1, the term in square brackets differs from unity by only 0.0056. Thus, the relative error in approximating $\langle T_{\theta z} \rangle$ by $\mu \gamma_s$ is 0.56%, a result which also follows directly from (4-14).

**4E.** *Radially nonuniform torsional deformations of annular specimens.* Conclusion 2 in Section 4C implies that for incompressible annular specimens a class of torsional deformations more general than *pure* torsion must be considered if both the outer and inner lateral surfaces ($r = R_o$ and $r = R_i$) are stress-free. Recall that the pure torsional deformation (4-7) does not involve any radial displacement. Here we briefly consider more general torsional deformations for which the annular specimen may deform radially:

$$r = \hat{r}(R), \qquad \theta = \Theta + \psi(Z - L), \qquad z = Z. \tag{4-26a}$$

Incompressibility requires that $1 = \det \boldsymbol{F} = (\partial r / \partial R)(r / R) = \partial(r^2) / \partial(R^2)$; consequently,

$$r = \sqrt{R^2 + \beta}, \tag{4-26b}$$

where $\beta$ is an arbitrary constant subject only to the condition that $R_i^2 + \beta > 0$. Note that the deformation (4-26) reduces to pure torsion ($r = R$) if and only if $\beta = 0$.

Proceeding as in the case of pure torsion, it can be shown that the deformation (4-26) is possible in any incompressible, isotropic elastic, annular specimen; that $T_{rz} = T_{r\theta} = 0$; and that the outer surface $R = R_o$ may be taken to be stress-free. This was first shown by Rivlin [1949].[35] The radial stress is expressed in terms of the undeformed radial coordinate by

$$T_{rr}(R) = -\int_R^{R_o} \mu \left[ \psi^2 \omega R + \frac{1}{R} - \frac{R^3}{(R^2 + \beta)^2} \right] dR \tag{4-27}$$

with the constitutive functions $\mu$ and $\omega$ generally dependent on $\psi^2$, $R^2$, and $\beta$. On letting $R = R_i$ in this relation and then setting the result to zero, we obtain an implicit relation for $\beta$ that must be satisfied in order that the inner surface $R = R_i$ is stress-free. Clearly, this value of $\beta$ depends on $\psi$, $R_i$, and $R_o$ as well as the constitutive functions $\mu$ and $\omega$. The dependence on $\mu$ drops out if $\mu$ is a constant as in the Mooney–Rivlin model. For that case, the integral can be evaluated and a simpler implicit relation for $\beta$ is obtained [Rivlin 1949, §8].[36]

**4F.** *Three-dimensional quasistatic torsion simulations.* Although the torsional deformation (4-26) is of some theoretical interest, in practice, it would be difficult to apply a torque on the face of a soft specimen while simultaneously admitting a radial deformation on that face. In the torsional Kolsky bar tests in [Nie et al. 2013], the faces of the specimen are glued to the bar and the load cell, and analogous

---

[35] Rivlin considered a slightly more general deformation that includes a superposed uniform axial extension. He assumed that the material is hyperelastic, but this condition is not necessary [Truesdell and Noll 1965, §57].

[36] Rivlin considered the more general case that includes a superposed uniform axial extension; see also (95.8) in [Truesdell and Noll 1965].

glued end conditions are used for their quasistatic torsion tests. Thus, for the actual torsion tests of interest here, neither the pure torsion considered in Sections 4B–4D nor the torsional deformation (4-26) can be expected to hold exactly. Nevertheless, it is clear from the discussion in Section 4E that, at axial locations between the two faces, an annular specimen will have a tendency to deform radially in order to satisfy the stress-free boundary conditions on the inner and outer surfaces. Since relatively short annular specimens are used, the constraints at either end of the specimen can be expected to severely restrict (though not completely eliminate) the radial deformation at axial locations in the interior. Thus, in quasistatic torsion tests with glued ends, we expect some axial variation in the radial deformation and consequently in the stress components as well as additional nonzero stress components such as $T_{rz}$. The analytical results for the torsional, axial, and hoop stresses in pure torsion may still hold approximately, but the accuracy of these approximations is not clear. Since a theoretical analysis of this problem is intractable,[37] we rely on numerical simulations for quantitative estimates of the stress state.

One face of the annular specimen was subjected to a rigid rotation while the other face was fixed so that material points on either face could not undergo axial or radial displacements. Stress-free boundary conditions were used on the outer surface $R = R_o$ and the inner surface $R = R_i$. Details of the numerical method are provided in Appendix A.

In these simulations, we used a compressible version of the Mooney–Rivlin model for the specimens.[38] The equation of state for the pressure in this model is

$$p = -\kappa \ln J \approx \kappa(1 - J), \qquad J = \det \boldsymbol{F}. \tag{4-28}$$

The constant $\kappa$ is the bulk modulus. The constitutive relation for the Cauchy stress tensor $\boldsymbol{T}$ is given by (4-2) with $\hat{p}$ and $\hat{\boldsymbol{S}}$ defined as follows:

$$\hat{p} = p + \tfrac{1}{3}\operatorname{tr}\hat{\boldsymbol{S}}, \qquad J\hat{\boldsymbol{S}} = \mu\big[\omega\widetilde{\boldsymbol{B}} - (1-\omega)\widetilde{\boldsymbol{B}}^{-1}\big] = 2C_1\widetilde{\boldsymbol{B}} - 2C_2\widetilde{\boldsymbol{B}}^{-1}. \tag{4-29}$$

Here $\mu$, $\omega$, $C_1$, and $C_2$ are constants as in the incompressible version, and

$$\widetilde{\boldsymbol{B}} = \frac{\boldsymbol{B}}{(\det \boldsymbol{B})^{1/3}} = \frac{\boldsymbol{B}}{J^{2/3}} \tag{4-30}$$

is the distortional part of the left Cauchy–Green tensor $\boldsymbol{B}$. Note that, regardless of the value of the Jacobian $J$, $\det \widetilde{\boldsymbol{B}} = \det \widetilde{\boldsymbol{B}}^{-1} = 1$, analogous to the conditions $\det \boldsymbol{B} = \det \boldsymbol{B}^{-1} = 1$ for the incompressible case. This relation for $\hat{\boldsymbol{S}}$ is identical to the relation (4-4) for the incompressible Mooney–Rivlin model except that $\boldsymbol{B}$ has been replaced by its distortional part and $\hat{\boldsymbol{S}}$ is multiplied by the factor $J$.[39] The relation $(4\text{-}29)_1$ for $\hat{p}$ guarantees consistency with $(4\text{-}3)_1$.

We used $\kappa = 2.3\,\text{GPa}$ for all simulations and varied the shear modulus by almost three orders of magnitude: $\mu = 800, 80, 8$, and $2\,\text{kPa}$. The corresponding ratios of bulk to shear modulus varied from 2875 to $1.15 \times 10^6$ so that in all cases the specimen was nearly incompressible. For each of the four values

---

[37] Some idea of the difficulty of this problem can be inferred from the paper [Hill and Lee 1989], which treats a slightly different problem, namely combined compression and torsion of incompressible, disc-shaped, Mooney–Rivlin specimens with glued ends. This work has been extended to torsional waves [Hill and Wegner 2004], but the results are not directly applicable to the dynamic problem considered here since annular specimens are not considered.

[38] Additional departures (perhaps small) from pure torsion will be introduced by the slight compressibility of the specimens.

[39] This factor ensures that the material is hyperelastic. The strain energy function is given by $W = \kappa J(\ln J - 1) + C_1(\operatorname{tr}\widetilde{\boldsymbol{B}} - 3) + C_2(\operatorname{tr}\widetilde{\boldsymbol{B}}^{-1} - 3)$.

of the shear modulus, simulations were performed for three values of the nondimensional parameter $\omega$: 0.3, 0.6, and 1. This resulted in twelve quasistatic simulations.

We have compared the stress states obtained from the numerical simulations (using the compressible version of the Mooney–Rivlin model) with the stress states that would have been obtained in pure torsion of an incompressible Mooney–Rivlin material (as determined from (4-22) and (4-24)). These comparisons are made at the same average angle of twist per unit length $\psi$ (equivalently, at the same average shear strain $\gamma_s$) and for the same set of twelve values for $\mu$ and $\omega$. The results are plotted in Figure 6. Each of the ten panels contains either thirteen or fifteen curves, but many (in panels $a$ and $b$, all of them) are indistinguishable. This is due (in part) to the normalization of the stress components as discussed in the next paragraph. In each panel, there are twelve curves for the numerical simulations (solid lines) and either one curve (panels $a$ and $b$) or three curves for the theoretical pure torsion (dashed lines).
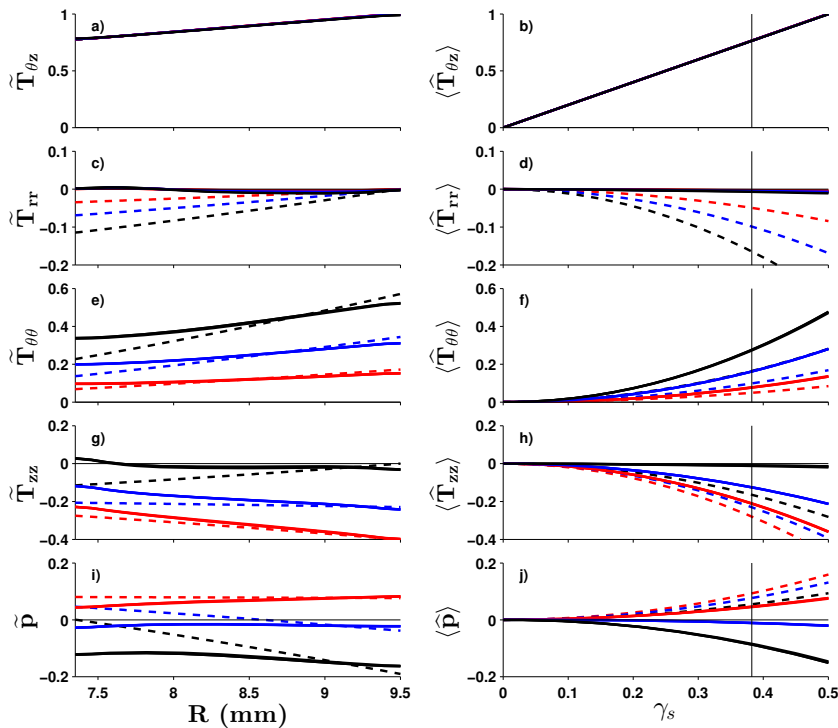


**Figure 6.** Normalized stress states in torsion for Mooney–Rivlin specimens. Twelve numerical simulations (solid lines) are compared with pure torsion (dashed lines). For each of four values of the shear modulus $\mu$ (800, 80, 8, and 2 kPa), curves for $\omega = 0.3$ (red), $\omega = 0.6$ (blue), and $\omega = 1.0$ (black) are shown. Curves for different shear moduli are indistinguishable (either approximately or exactly) because of the normalizations. The left panels examine the variation of the normalized stress with referential radius for an angle of twist per unit length $\psi = 0.059$ radians/mm at the axial location $Z = L/2$. The right panels are plots of normalized volume-averaged stress versus average shear strain. The vertical line in the right column indicates the average shear strain for the panels on the left.

In order to condense the information from the simulations and the theoretical results and also to more clearly display the relative magnitude of the stresses in each case, all stress components in Figure 6 have been normalized by an appropriate "maximum" torsional stress. For the left column, the tilde on the stresses indicates that they have been normalized by $\mu \psi R_o$, which by (4-16)$_1$ is the maximum torsional stress that would occur in a pure torsional deformation. For the right column, the hat on the stresses indicates that they have been normalized by the volume-averaged torsional stress $\langle T_{\theta z} \rangle$ (see (4-25)) that would occur in a pure torsional deformation, evaluated at the final average shear strain $\gamma_s = 0.5$. The angle brackets on the stresses in the right column indicate that these normalized stresses have then been volume-averaged.

In the left column of Figure 6, we examine the radial variation in the torsional stress, the normal stress components, and the pressure at an axial location in the middle of the specimen ($Z = L/2$). In these plots, the average angle of twist per unit length is $\psi = 0.059\,\text{radians/mm} = 3.38°/\text{mm}$, and the corresponding average shear strain is $\gamma_s = 0.38$. Data from torsion tests is typically plotted as average shear stress versus average shear strain $\gamma_s$ with the average shear stress inferred from the measured torque. The right column of Figure 6 displays the volume-averaged stress-strain curves. The vertical black lines in the right column indicate the average shear strain (0.38) for the panels on the left.

Consider panel $a$ for the radial variation of the torsional stress. Since $T_{\theta z} = \mu \psi r$ for pure torsion of an incompressible Mooney–Rivlin material, the normalized torsional stress in this case is given by $\widetilde{T}_{\theta z} = \mu \psi r / \mu \psi R_o = r/R_o = R/R_o$, independent of $\mu$ or $\omega$. Thus, for pure torsion of an incompressible Mooney–Rivlin material, there is a single normalized torsional stress versus radius curve, namely the line $R/R_o$. This line and the twelve normalized torsional stress versus radius curves from the numerical simulations are indistinguishable, the maximum relative difference being less than 1%.

A similar situation occurs for the average torsional stress versus average shear strain curves in panel $b$. Since $\langle T_{\theta z} \rangle$ is given by (4-25) for pure torsion of an incompressible Mooney–Rivlin material, the normalized average torsional stress in this case is given by $\langle \widehat{T}_{\theta z} \rangle = \gamma_s / (\gamma_s|_{0.5})$. Thus, for pure torsion of an incompressible Mooney–Rivlin material, there is a single normalized average torsional stress versus average strain curve, namely the line $\gamma_s/0.5$. This line and the twelve normalized average torsional stress versus average shear strain curves from the numerical simulations are indistinguishable, the maximum relative difference again being less than 1%.

Thus, even though the annular specimens in our numerical simulations cannot undergo a pure torsional deformation, the torsional stress in those simulations is indistinguishable from the torsional stress in theoretical pure torsion of an incompressible Mooney–Rivlin material. On the other hand, it is clear from Figure 6 that this conclusion does not hold for the normal stress components; that is, the normal stresses and the pressure in the annular specimen simulations (solid lines) do not agree with the theoretical predictions for pure torsion of an incompressible Mooney–Rivlin material (dashed lines).

For pure torsion of an incompressible Mooney–Rivlin material, the theoretical relations (4-22) and (4-24) predict that the normal stress components and the pressure are proportional to the shear modulus $\mu$ and depend on $\omega$ as well; consequently, the normalized stress components in panels $c$–$j$ in Figure 6 are independent of $\mu$ but still depend on $\omega$. This results in three normalized stress curves (dashed lines) for the case of pure torsion in each of these panels — one curve for each of the three values of $\omega$.

The disagreement between the normalized stresses for pure torsion and those for the numerical simulations are most pronounced for the radial component (panels $c$ and $d$). In fact, the normalized radial

stresses for the simulations are so small that all twelve curves (solid lines) are indistinguishable from the horizontal axis ($\widetilde{T}_{rr} = 0$ or $\langle \widetilde{T}_{rr} \rangle = 0$). Of course, the fact that the radial stress is essentially zero throughout the annular specimen is not unexpected in view of the fact that it is zero on the inner and outer lateral surfaces. This is one of the motivations for using annular specimens. The other motivation for using annular (as opposed to disc-shaped) specimens in torsion tests is that, while torsional stress $T_{\theta z}$ and the shear strain $E_{\theta z}$ are radially nonuniform, the total radial variation in these quantities is expected to be smaller for annular specimens. For the torsional stress, this is verified in Figure 6a.

Unlike the radial stresses, the hoop stress, axial stress, and pressure (panels e–j) for the simulations (solid lines) share some qualitative features with the theoretical predictions for pure torsion (dashed lines). In particular, the normalized hoop stress, axial stress, and pressure for the simulations are (approximately) independent of the shear modulus but depend strongly on the value of $\omega$ so that the twelve curves appear to collapse into three curves. Furthermore, for both the simulations and the pure torsion case, the hoop stress increases with increasing $\omega$ while the magnitude of the axial stress decreases with increasing $\omega$. For the axial and hoop stresses, the discrepancies between the simulations and the pure torsion case increase with increasing $\omega$.

Further consideration of (4-16) and (4-22) shows that, for pure torsion, the ratio of normal stress to torsional shear stress increases with shear strain: the shear stress depends linearly on $\psi$ while the normal components depend quadratically on $\psi$ and thus quadratically on the average shear strain $\gamma_s$. Comparison of the solid curves in panel b with those in panels f and h in Figure 6 shows that the same conclusion holds for the hoop and axial stresses (but not the radial stress) in the numerical simulations. Thus, for sufficiently large angles of twist or for sufficiently thin specimens, the magnitude of the normal stresses could exceed the shear stress. On the other hand, a smaller shear strain of 0.2, say, gives an average hoop stress that is only 5 to 20% of the shear stress (depending on $\omega$) and an average axial stress that is only 1 to 15% of the shear stress.

The glued-end boundary conditions in combination with the stress-free boundary conditions on the inner and outer surfaces of the annular specimen resulted in axial variations in the stress components in the torsion simulations although these results are not plotted here. For the normal stresses, these axial variations were concentrated within approximately 0.25 mm of either face of the specimen and essentially vanished away from the specimen faces. Both hoop and axial stresses varied by as much as 30% near the faces whereas the variation in this region for the torsional stress $T_{\theta z}$ was typically less than 5%. The other shear components, $T_{rz}$ and $T_{r\theta}$, were also nonzero. They were smaller in magnitude (typically less than 10% of the torsional stress) and varied throughout the length of the specimen.

Although the magnitude of $T_{rz}$ is small, the fact that $T_{rz}$ cannot be identically zero can be established as follows. Using the assumption that the specimen is in equilibrium (so that div $\boldsymbol{T} = \boldsymbol{0}$) together with the stress-free boundary conditions on the inner and outer surfaces of the annular specimen, one could show

$$\int_{\mathcal{A}(z)} \frac{1}{r} T_{\theta\theta} \, dA = \frac{\partial}{\partial z} \int_{\mathcal{A}(z)} T_{rz} \, dA, \qquad (4\text{-}31)$$

where $\mathcal{A}(z)$ is the annular cross-section at the axial location $z$.[40] As observed above (see panel e in

---

[40] We omit the proof of this relation. It is a fairly general result in the sense that no material symmetry conditions are required, the specimen need not be homogeneous, and neither the initial nor deformed annular cross-sections need be axially uniform or have circular boundaries.

Figure 6), $T_{\theta\theta}$ is positive at each radial location. Hence, the integral on the left above is positive and must be balanced by an axial gradient in the integral of $T_{rz}$ over the cross-section $\mathcal{A}(z)$.

## 5. Three-dimensional dynamic simulations

In this section, we further supplement our one-dimensional dynamic simulations and three-dimensional quasistatic analysis and simulations with three-dimensional dynamic simulations. Our dynamic torsion simulations use the same glued-end boundary conditions and stress-free boundary conditions on the outer and inner surfaces as in the quasistatic simulations discussed in Section 4F. With the exception of the viscoelastic results discussed in Section 5B, we used the same constitutive model and the same model parameters as in the three-dimensional quasistatic simulations except that the $\mu = 2\,\mathrm{kPa}$ case is not considered. Thus, we used $\kappa = 2.3\,\mathrm{GPa}$ and varied the shear modulus by two orders of magnitude: $\mu = 800$, 80, and 8 kPa. The corresponding ratios of bulk to shear modulus varied from 2875 to $2.875 \times 10^5$ so that in all cases the specimen was nearly incompressible. For each of the three values of the shear modulus, simulations were performed for three values of the nondimensional parameter $\omega$: 0.3, 0.6, and 1. The nine simulations used the same 700/s loading pulse as the one-dimensional *Simulations I–III*; see Table 2 and panels *a* and *b* in Figure 3. Details of the numerical method are provided in Appendix A.

**5A.** *Nonlinear elastic model for the specimen.* We calculated the radially averaged stress at the *Load Cell* for each of the six components $T_{ij}$ of the stress tensor, i.e.,

$$\frac{1}{\pi(R_o^2 - R_i^2)} \int_{R_i}^{R_o} T_{ij}(R, L)2\pi R\, \mathrm{d}R.$$

These time histories are plotted for the nine simulations in Figure 7. The shear modulus $\mu$ changes with the row, and $\omega$ changes with the column so that the nine panels span vastly different elastic responses.

In the quasistatic torsion simulations (see Figure 6), the torsional shear stress $T_{\theta z}$ is insensitive to the dimensionless parameter $\omega$ in the Mooney–Rivlin model. This is also observed in the dynamic case: comparing the shear stress $T_{\theta z}$ (green traces) for fixed shear modulus, i.e., panels *a–c*, *d–f*, and *g–i* in Figure 7, we see little to no variation with $\omega$. Similarly, in both the quasistatic and dynamic simulations, the magnitude of the axial stress $T_{zz}$ (black traces) decreases with increasing $\omega$ whereas the hoop stress $T_{\theta\theta}$ (blue traces) increases with increasing $\omega$ with the exception of the hoop stress for the $\mu = 8\,\mathrm{kPa}$ dynamic case. Since neither $T_{zz}$ or $T_{\theta\theta}$ is measured in a Kolsky bar test, there would be no way to infer a value for $\omega$ from the test data, namely the measured shear stress, even if it were known that the specimen behavior was governed by the Mooney–Rivlin model.

Unlike the quasistatic simulations, for a given value of $\omega$, the relative magnitude of the normal and torsional shear stress components vary considerably with the shear modulus in the dynamic simulations. In particular, the radial stress (red traces) is not negligible for the $\mu = 80$ and 8 kPa dynamic simulations. Also note that, for the $\mu = 8\,\mathrm{kPa}$ case with $\omega = 0.3$ or 0.6 (panels *g* and *h*), all three normal stress components begin to change well before the torsional stress increases. This effect cannot be due to bending waves or longitudinal waves that might be generated in the incident bar as a result of the initial impact since such effects are not included in the simulations. Rather, it is caused by a longitudinal precursor wave in the specimen as discussed in the next paragraph. From Section 3, it is clear that
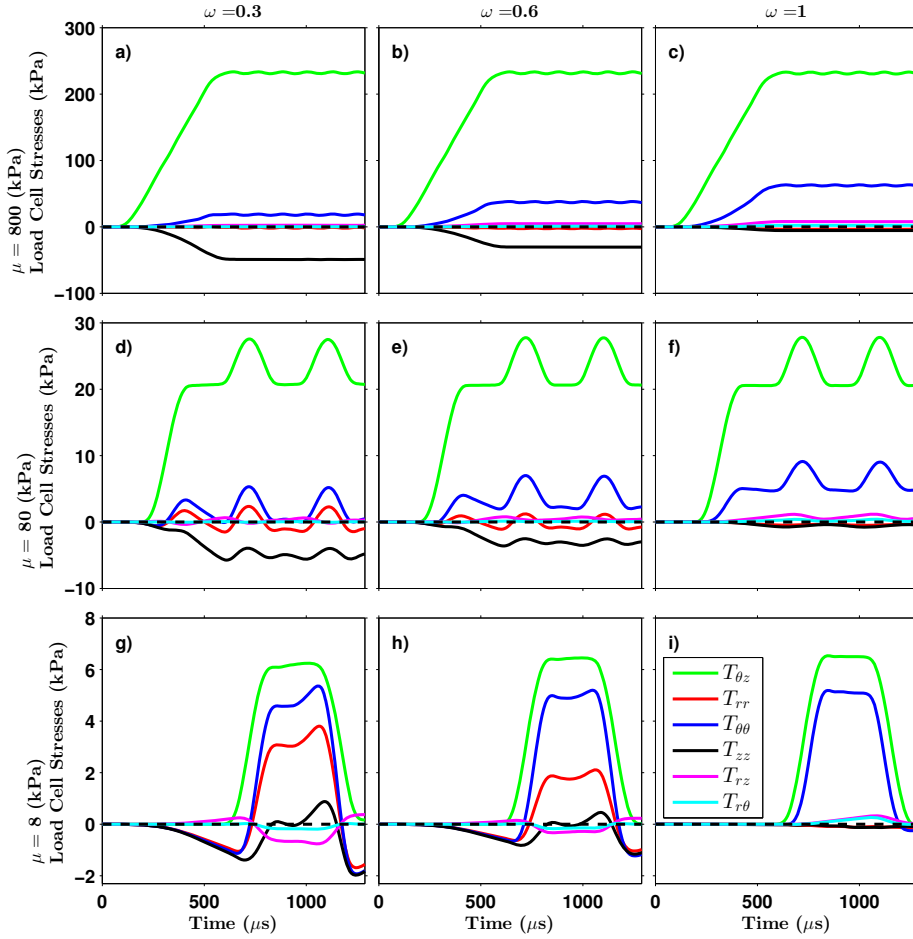
**Figure 7.** The radially averaged stress components at the *Load Cell* ($Z = L$) versus time for the nine simulations: two decades of shear modulus ($\mu = 800$, 80, and 8 kPa) and three values of dimensionless parameter ($\omega = 0.3$, 0.6, and 1.0). All simulations used the same 700/s loading pulse as the one-dimensional *Simulations I–III*; see Table 2 and panels *a* and *b* in Figure 3. The legend for the line colors is given in panel *i* and is consistent throughout the figure. Note the change in vertical scales for the different rows.

dynamic equilibrium is not reached when $\mu \leq 80$ kPa, and the three-dimensional simulations inform us that the stress state is no longer simple as well.

The normal stresses produced by the shearing deformation propagate at the longitudinal elastic wave speed,[41] which far exceeds the shear wave speed for all cases in Figure 7. Indeed, the longitudinal wave speed is about 1.52 mm/$\mu$s for all nine cases.[42] Hence, this wave arrives at the *Load Cell* in about 1.1 $\mu$s,

---

[41]This is a well-known nonlinear elastic effect [Davison 1966; Abou-Sayed and Clifton 1976; Scheidler 1998].

[42] For a nonlinear elastic solid, a longitudinal wave propagating into undeformed material travels at the linear elastic wave speed $c_L = \sqrt{\frac{4}{3}c_S^2 + c_B^2}$, where $c_S$ is the shear wave speed and $c_B$ is the bulk wave speed, i.e., $\sqrt{\kappa/\rho}$. For the bulk and shear moduli considered here ($\kappa = 2.3$ GPa and $\mu \leq 800$ kPa), the shear wave speed is negligible and $c_L \approx c_B = 1.52$ mm/$\mu$s.

which is essentially instantaneous on the time scale of Figure 7. But even though the normal stresses begin to change at the *Load Cell* at this early time, their magnitude is initially quite small — on the order of the square of the shear strain produced by the slower torsional wave. Consequently, these initial changes cannot be observed on the scale of the plots until much later times. And it is only in panels *g* and *h* that the magnitude of the normal stresses (relative to the torsional stress) is significant enough to be observed prior to the arrival of the torsional wave.

**5B.** *Nonlinear viscoelastic model for the specimen.*  Although the goal of the torsional Kolsky bar test considered here is to quantify the strain-rate sensitivity of viscoelastic soft tissues, only elastic constitutive models have been considered up to this point. Elastic models (linear or nonlinear) are particularly useful for revealing inertial effects: since the stress in an elastic material is rate-independent, any differences between the quasistatic and dynamic simulations of the torsion test must necessarily be due to inertial effects. There is certainly no reason to expect that these inertial effects will disappear for materials exhibiting viscoelastic response. Nevertheless, we have also performed some three-dimensional dynamic simulations of torsional Kolsky bar tests using a nonlinear viscoelastic constitutive model[43] for the specimen.

We used an equilibrium elastic shear modulus of 2 kPa and an instantaneous elastic shear modulus of 40 kPa,[44] five times larger than the 8 kPa shear modulus that had been used as representative of brain tissue in the elastic models. This gives a viscoelastic shear wave speed about 2.2 times the shear speed for the $\mu = 8$ kPa linear and nonlinear elastic cases.[45]  It should be clear from our results for these elastic cases that this wave speed is much too slow for dynamic equilibrium to be achieved. Indeed, while the stress histories in our simulations with the viscoelastic model differed both qualitatively and quantitatively from those described above for the elastic model, we found that the viscoelastic stress histories fell roughly between the $\mu = 80$ kPa and 8 kPa elastic cases in Figure 7.

## 6. Discussion and conclusions

We have conducted one- and three-dimensional analyses and simulations to understand the deformations and stress states that exist in nearly incompressible soft materials in a torsional Kolsky bar test. Here we highlight the main conclusions of this study and also discuss some relevant issues that were not addressed previously.

*The use of* (*linear or nonlinear*) *elastic constitutive models for the specimen in numerical simulations of Kolsky bar tests can reveal the presence of inertial effects.* Using viscoelastic models in

---

[43] See Appendix A for more details.

[44] This is close to our rough estimate of 42 kPa for the 700/s tests in [Nie et al. 2013]; see the discussion at the end of Section 3D. Recall that they estimated an initial shear modulus of 53.5 kPa from their average "700/s" shear stress versus shear strain curve.

[45] For a (linear or nonlinear) viscoelastic material, the speed of a shear wave propagating into an undeformed region is that of a linear elastic material with shear modulus equal to the (small strain) instantaneous elastic shear modulus of the viscoelastic material. This result also holds for any simple material with fading memory [Coleman et al. 1965]. However, the shear wave in the torsion test initially propagates into a slightly deformed region caused by the longitudinal precursor wave and then reflects from the *Load Cell* into a more complicated strain state. Nevertheless, the shear wave speed into an undeformed material should yield a rough estimate for the wave speed in this test, and for the viscoelastic model considered here, this is $\sqrt{40\,\text{kPa}/\rho} = \sqrt{5 \times 8\,\text{kPa}/\rho}$ or $\sqrt{5}$ times the shear speed for the $\mu = 8$ kPa elastic cases.

these simulations will add strain-rate effects to the stress histories but not substantially alter the inertial effects since the main issue here is the slow shear wave speed in the specimen.

*In soft specimens, the travel time of the torsional wave can be on the order of the loading pulse duration, in which case there is insufficient time for ring-up to dynamic equilibrium. For the torsional Kolsky bar tests on bovine brain tissue at a strain-rate of "700/s" that were reported in* [Nie et al. 2013]*, the specimen could not have been in dynamic equilibrium, contrary to statements made in that paper.* Consequently, their "stress-strain curves" are not valid — the average strain used in their plots does not correspond to the strain at the load cell. In fact, throughout much of the test, the actual strain at the load cell was likely several times larger than the average strain used in their stress-strain plots.

*The stress history at the load cell should never be time-shifted to synchronize it with the history of the average strain in order to produce a "stress-strain curve".* If the stress-strain curves produced from unshifted data contain an initial strain interval for which the stress is zero (as in the left panels in Figure 4), then this is a clear indication that the specimen is not in dynamic equilibrium and consequently that no meaningful stress-strain curves can be inferred from the test data. Even if the "stress-strain curves" produced by time-shifting the load cell data *appear* physically reasonable, they will necessarily contain erroneous "strain-rate effects".

*It is not clear how to modify the experimental design to alleviate the inertial effects that exist when testing with very soft specimens at high strain-rates.* In Section 3E, we discussed the changes in the loading pulse and the specimen geometry that would be necessary to improve the quality. These alterations require longer bars, thinner specimens, and reductions of the maximum strain-rates considered. Ignoring the practical difficulties that longer bars, polymer bars, or thinner specimens pose, the lower strain-rates required would be on the order of 100–200/s (unless larger strains are considered) and are perhaps too low for the ranges needed for the modeling effort.

*Other Kolsky bar tests such as double-lap shear* [Saraf et al. 2007; Trexler et al. 2011] *or circular shearing* [Nie et al. 2011] *will have similar issues with dynamic equilibrium.* Similar dimensional arguments can be made for each of these tests. With proper consideration of the direction of the shear wave propagation and the relevant specimen length, the results of Section 3 would apply. Thus, inertial effects are still an issue with high shear strain-rate Kolsky bar tests on soft materials.

In view of the remarks above, *for tests on sufficiently soft specimens at sufficiently high strain-rates, experimenters should abandon the practice of presenting their data as "stress-strain curves" and simply report the measurements that are valid.* For the torsional Kolsky bar test of Nie et al. [2013], this consists of the torque history at the load cell and the history of the angle of twist at the other face of the specimen. These histories should be provided for each valid test, not averaged over multiple tests. Such data, in conjunction with numerical simulations of the tests, could be used in the process of validating a constitutive model that has already been calibrated. In this regard, *optical measurements of the angle of twist at the end of the incident bar adjacent to the specimen should be used in place of the traditional strain gage measurements on the incident bar.* Unlike the analysis of strain gage data, the analysis of optical data does not require that the specimen be in dynamic equilibrium or that the incident and reflected pulses do not overlap at the measurement location.

*The above procedure could not be used to actually calibrate the parameters in a viscoelastic constitutive model unless the twist and torque histories are part of a larger data set for use with a numerical inverse method.* The issue here is nonuniqueness, for which there are several sources. Even if a numerical

inverse method were used to optimize the fit to the measured stress and twist histories, it seems likely that several different calibrations might fit the limited data equally well, particularly in view of the variability that exists in biological specimens and the fact that several reasonable criteria for optimality could be used. Each calibration would likely result in a different numerical prediction of the strain history at the load cell. Since this strain history cannot be measured in the torsional Kolsky bar test, there would be no criterion for selecting one of these calibrations over the other. Also, significant radial, hoop, and axial stresses exist if the specimen is sufficiently soft and the strain-rate sufficiently high, yet these normal stress components are not measured in the torsional Kolsky bar test.[46] Furthermore, the measured torque (or the torsional shear stress $T_{\theta z}$) may be insensitive to some of the parameters that determine these normal stresses as was demonstrated for the case of a Mooney–Rivlin model. Different model calibrations might fit the twist and torque histories equally well or nearly as well and yet predict drastically different normal stresses, but there would be no way to determine which (if any) of these predictions are correct.

## Appendix A: Details of numerical methods

***One-dimensional dynamic.*** We solve the wave equation (3-8) along with boundary conditions (3-3)$_1$ and (3-12) numerically using a finite difference scheme. Initially, an explicit second-order, centered-time and centered-space method was implemented. This method produced reasonable results but had a tendency to be dispersive, creating erroneous ripples and other small oscillatory noise. The results presented here use a Crank–Nicolson method applied to the centered-space differences, thus making it a semi-implicit method; i.e., the approximations of the spatial derivatives were taken as an average of the values for the current time step and the next time step. This alteration trades the dispersive error for a slightly dissipative error. The length of the specimen ($L = 1.7$ mm) was divided up into equal intervals ($\Delta z = 0.0085$ mm) so that $u(z, t)$ was evaluated at 200 points; a time step $\Delta t$ was chosen to satisfy the Courant stability criterion for the explicit method, $c\Delta t/\Delta z \leq 1$.

***Three-dimensional quasistatic.*** Meshes were generated in Cubit (V12.1, Sandia National Laboratory). Simulations were performed using Sierra SolidMechanics (Adagio 4.24, Sandia National Laboratory). Adagio is an implicit, nonlinear preconditioned conjugate gradient solver. Reduced integration on HEX8 element meshes was performed. Due to the highly constrained nature of the problem, extreme care had to be taken to ensure the mesh was structured and symmetric to prevent mesh artifacts. Postprocessing of simulation results was carried out in ParaView (V3.14.0, Kitware) and MATLAB (The MathWorks).

The solutions obtained from the fully three-dimensional simulations were rotationally symmetric and enabled a reduction of the data. Variables were evaluated along five radial lines at a single angle and equally spaced axial locations ($\Theta = 0$ and $Z = 0, \frac{1}{4}L, \frac{1}{2}L, \frac{3}{4}L, L$). This postprocessing was performed in ParaView to enable further analysis. The area integrals used a composite Simpson's method in MATLAB. Similarly, volumetric averages were calculated from the five area integrals utilizing a five-point Simpson rule. Continuous plots over the radius of the specimens have been linearly interpolated between elements.

***Three-dimensional dynamic.*** Several demanding simulation requirements arise when modeling shear wave propagation in soft, nearly incompressible materials. Figure 3 (for the one-dimensional simulations)

---

[46] Measurements of axial stress in quasistatic torsion tests are common, and such measurements could perhaps be done in torsional Kolsky bar tests as well. However, it seems unlikely that radial or hoop stresses could ever be measured.

shows that, when a specimen is far from dynamic equilibrium, large gradients in strain exist. These large gradients cannot be captured in a numerical simulation without a sufficiently fine mesh. In *Simulation I*, there were changes in strain of 0.4 over distances of approximately 0.6 mm. A large number of elements along the shortest dimension of the specimen geometry requires extremely large meshes to model the entire specimen in a three-dimensional simulation. A large reduction in the number of elements is gained by utilizing the rotational symmetry of the problem and effectively changing it to a two-dimensional problem by simulating a thin wedge with periodic boundaries. An explicit code would require very short time steps for these small elements. Simulations were performed using Adagio with HHT integration [Hilber et al. 1977]. This enabled taking larger time steps while maintaining stability and introducing a small damping to higher frequencies.

The software used for meshing and postprocessing was the same as for the quasistatic simulations. Utilizing the rotational symmetry of the problem, variables were evaluated along axial lines at a single angle ($\Theta = 0$) and five equally spaced radial locations from $R_i$ to $R_o$. For the simulations with a viscoelastic specimen, we used the Viscoelastic Swanson Model in Sierra SolidMechanics. The parameters in the elastic part of that model were chosen so that it reduced to a Mooney–Rivlin model.

## Appendix B: Mathematical formulation of a smooth loading pulse

The simulations of the torsional Kolsky bar test require a loading pulse (i.e., an applied average strain-rate history $\dot{\gamma}_s$) that ramps up smoothly to a constant value before subsequently unloading (Figure 2a). In this appendix, we formulate a parametrized loading pulse using a Hermitian smoothing spline. The time integral of the average strain-rate $\dot{\gamma}_s$ can then be used to obtain an applied average shear strain $\gamma_s$ and ultimately the applied displacement boundary condition (2-6).

We use a Hermitian smoothing spline of degree 5 as the basis for the ramp-up portion of the loading pulse (see [Fitzpatrick and Scheidler 2013]):

$$H_5(x) = 10x^3 - 15x^4 + 6x^5, \quad 0 \le x \le 1. \tag{B-1}$$

This function increases from 0 at $x = 0$ to 1 at $x = 1$ and has zero first and second derivatives at both of these end points. Following [Fitzpatrick and Scheidler 2013], one can use $H_5(x)$ to construct a strain-rate function that ramps up from zero to $\dot{\gamma}_{max}$ over the time interval $[0, t_r]$, maintains this constant value over the time interval $[t_r, t_r + t_p]$, and then unloads to zero over the time interval $[t_r + t_p, t_d]$:

$$\dot{\gamma}_s(t) = \begin{cases} 0, & t < 0, \\ \dot{\gamma}_{max} H_5\left(\dfrac{t}{t_r}\right), & 0 \le t \le t_r, \\ \dot{\gamma}_{max}, & t_r < t < t_r + t_p, \\ \dot{\gamma}_{max}\left[1 - H_5\left(\dfrac{t - (t_r + t_p)}{t_r}\right)\right], & t_r + t_p \le t \le t_d, \\ 0, & t > t_d. \end{cases} \tag{B-2}$$

Here $t_r$ is referred to as the rise time, i.e., the time it takes to reach a constant strain-rate, $t_p$ is the duration of the constant strain-rate plateau, and $t_d$ is the total duration of the pulse. In the simulations, we made the additional assumption that the loading pulse is symmetric; that is, the unloading duration $t_d - (t_r + t_p)$ equals the rise time so that $t_d = 2t_r + t_p$.

Note that

$$\dddot{\gamma}_s(0) = \dddot{\gamma}_s(t_r) = \dddot{\gamma}_s(t_r + t_p) = 0, \qquad \ddddot{\gamma}_s(0) = \ddddot{\gamma}_s(t_r) = \ddddot{\gamma}_s(t_r + t_p) = 0. \tag{B-3}$$

Since $\dddot{\gamma}_s$ and $\ddddot{\gamma}_s$ are identically zero during the constant strain-rate plateau as well as for $t < 0$ and $t > t_d$, the conditions (B-3) guarantee that $\dot{\gamma}_s$ is twice continuously differentiable. This degree of smoothness was necessary to avoid an unwanted ringing in the simulations that would otherwise result from a lower order polynomial.

An explicit expression for $\gamma_s(t)$ is rather messy, and in practice, it is simpler to work with the integral of $H_5$:

$$\mathbb{H}_5(x) = \int_0^x H_5(y)\, dy = x^4\left(x^2 - 3x + \tfrac{5}{2}\right). \tag{B-4}$$

Integrating each case in (B-2) with respect to time, assuming a symmetric loading pulse, and using $\mathbb{H}_5(1) = \tfrac{1}{2}$ gives

$$\gamma_s(t) = \begin{cases} 0, & t < 0, \\ \dot{\gamma}_{max} t_r \mathbb{H}_5\left(\dfrac{t}{t_r}\right), & 0 \le t \le t_r, \\ \dot{\gamma}_{max}\left[\tfrac{1}{2}t_r + (t - t_r)\right], & t_r < t < t_r + t_p, \\ \dot{\gamma}_{max}\left[\tfrac{1}{2}t_r + (t - t_r) - t_r \mathbb{H}_5\left(\dfrac{t - (t_r + t_p)}{t_r}\right)\right], & t_r + t_p \le t \le 2t_r + t_p, \\ \dot{\gamma}_{max}[t_r + t_p], & t > 2t_r + t_p = t_d. \end{cases} \tag{B-5}$$

Equations (B-2) and (B-5) are smooth functions that qualitatively reproduce typical strain and strain-rate loading conditions generated in Kolsky bar tests.

## Acknowledgements

## References

[Abou-Sayed and Clifton 1976]  A. S. Abou-Sayed and R. J. Clifton, "Pressure shear waves in fused silica", *J. Appl. Phys.* **47**:5 (1976), 1762–1770.

[Batra 2006]  R. C. Batra, *Elements of continuum mechanics*, American Institute of Aeronautics and Astronautics, Reston, VA, 2006.

[Beatty 1987]  M. F. Beatty, "Topics in finite elasticity: Hyperelasticity of rubber, elastomers, and biological tissues—with examples", *Appl. Mech. Rev. (ASME)* **40**:12 (1987), 1699–1734.

[Chen and Song 2011]  W. Chen and B. Song, *Split Hopkinson (Kolsky) bar: Design, testing and applications*, Springer, New York, 2011.

[Coleman et al. 1965]  B. D. Coleman, M. E. Gurtin, and I. Herrera, "The velocity of one-dimensional shock and acceleration waves", pp. 1–19 in *Wave propagation in dissipative materials*, Springer, Berlin, 1965.

[Davison 1966] L. Davison, "Propagation of plane waves of finite amplitude in elastic solids", *J. Mech. Phys. Solids* **14**:5 (1966), 249–270.

[Donnelly and Medige 1997] B. R. Donnelly and J. Medige, "Shear properties of human brain tissue", *J. Biomech. Eng.* (*ASME*) **119**:4 (1997), 423–432.

[Fitzpatrick and Scheidler 2013] J. Fitzpatrick and M. Scheidler, "Considerations for numerical modeling of dynamic behavior of soft materials", pp. 29–39 in *Dynamic behavior of materials, I* (Costa Mesa, CA, 2012), edited by V. Chalivendra et al., Springer, New York, 2013.

[Gilat 2000] A. Gilat, "Torsional Kolsky bar testing", pp. 505–515 in *Mechanical testing and evaluation*, 10th ed., edited by H. Kuhn and D. Medlin, ASM Handbook **8**, ASM International, Materials Park, OH, 2000.

[Graff 1975] K. F. Graff, *Wave motion in elastic solids*, Ohio State University Press, Columbus, OH, 1975.

[Gray 2000] G. T. Gray, "Classic split-Hopkinson pressure bar testing", pp. 462–476 in *Mechanical testing and evaluation*, 10th ed., edited by H. Kuhn and D. Medlin, ASM Handbook **8**, ASM International, Materials Park, OH, 2000.

[Green and Adkins 1960] A. E. Green and J. E. Adkins, *Large elastic deformations*, Clarendon Press, Oxford, 1960.

[Hartley et al. 1985] K. A. Hartley, J. Duffy, and R. H. Hawley, "The torsional Kolsky (split Hopkinson) bar", pp. 218–228 in *Mechanical testing*, 9th ed., edited by J. R. Newby, Metals Handbook **8**, American Society for Metals, Metals Park, OH, 1985.

[Hilber et al. 1977] H. M. Hilber, T. J. R. Hughes, and R. L. Taylor, "Improved numerical dissipation for time integration algorithms in structural dynamics", *Earthq. Eng. Struct. Dyn.* **5**:3 (1977), 283–292.

[Hill and Lee 1989] J. M. Hill and A. I. Lee, "Combined compression and torsion of circular cylindrical pads of rubber", *J. Mech. Phys. Solids* **37**:2 (1989), 175–190.

[Hill and Wegner 2004] J. M. Hill and J. L. Wegner, "New families of exact nonlinear waves for the neo-Hookean finite elastic solid", *Math. Mech. Solids* **9**:1 (2004), 81–95.

[Hrapko et al. 2006] M. Hrapko, J. A. W. van Dommelen, G. W. M. Peters, and J. S. H. M. Wismans, "The mechanical behaviour of brain tissue: Large strain response and constitutive modelling", *Biorheology* **43**:5 (2006), 623–636.

[Miller and Chinzei 1997] K. Miller and K. Chinzei, "Constitutive modelling of brain tissue: Experiment and theory", *J. Biomech.* **30**:11-12 (1997), 1115–1121.

[Mooney 1940] M. Mooney, "A theory of large elastic deformation", *J. Appl. Phys.* **11**:9 (1940), 582–592.

[Nicolle et al. 2004] S. Nicolle, M. Lounis, and R. Willinger, "Shear properties of brain tissue over a frequency range relevant for automotive impact situations: New experimental results", *Stapp Car Crash J.* **48** (2004), 239.

[Nie et al. 2011] X. Nie, R. Prabhu, W. W. Chen, J. M. Caruthers, and T. Weerasooriya, "A Kolsky torsion bar technique for characterization of dynamic shear response of soft materials", *Exp. Mech.* **51**:9 (2011), 1527–1534.

[Nie et al. 2013] X. Nie, B. Sanborn, T. Weerasooriya, and W. Chen, "High-rate bulk and shear responses of bovine brain tissue", *Int. J. Impact Eng.* **53** (2013), 56–61.

[Rivlin 1947] R. S. Rivlin, "Torsion of a rubber cylinder", *J. Appl. Phys.* **18**:5 (1947), 444–449.

[Rivlin 1948a] R. S. Rivlin, "Some applications of elasticity theory to rubber engineering", pp. 1–8 in *Proceedings of the 2nd Rubber Technology Conference* (London, 1948), edited by T. R. Dawson, Heffer, Cambridge, 1948.

[Rivlin 1948b] R. S. Rivlin, "Large elastic deformations of isotropic materials, IV: Further developments of the general theory", *Phil. Trans. R. Soc. A* **241**:835 (1948), 379–397.

[Rivlin 1949] R. S. Rivlin, "Large elastic deformations of isotropic materials, VI: Further results in the theory of torsion, shear and flexure", *Phil. Trans. R. Soc. A* **242**:845 (1949), 173–195.

[Rivlin and Saunders 1951] R. S. Rivlin and D. W. Saunders, "Large elastic deformations of isotropic materials, VII: Experiments on the deformation of rubber", *Phil. Trans. R. Soc. A* **243**:865 (1951), 251–288.

[Sanborn 2011] B. Sanborn, *An experimental investigation of radial deformation of soft materials in Kolsky bar experiments*, Masters thesis, Purdue University, 2011, Available at http://search.proquest.com/docview/904409338.

[Sanborn et al. 2012] B. Sanborn, X. Nie, W. Chen, and T. Weerasooriya, "Inertia effects on characterization of dynamic response of brain tissue", *J. Biomech.* **45**:3 (2012), 434–439.

[Saraf et al. 2007]  H. Saraf, K. T. Ramesh, A. M. Lennon, A. C. Merkle, and J. C. Roberts, "Measurement of the dynamic bulk and shear response of soft human tissues", *Exp. Mech.* **47**:3 (2007), 439–449.

[Scheidler 1998]  M. Scheidler, "Response of nonlinear elastic solids to oblique plate impact", pp. 921–924 in *The tenth American Physical Society topical conference on shock compression of condensed matter* (Amherst, MA, 1997), edited by S. C. Schmidt et al., AIP Conf. Proc. **429**, American Institute of Physics, New York, 1998.

[Scheidler and Kraft 2010]  M. Scheidler and R. Kraft, "Inertial effects in compression Hopkinson bar tests on soft materials", in *Proceedings of the ARL ballistic protection technologies workshop* (Herndon, VA, 2010), Army Research Laboratory, Adelphi, MD, 2010.

[Scheidler et al. 2011]  M. Scheidler, J. Fitzpatrick, and R. Kraft, "Optimal pulse shapes for SHPB tests on soft materials", pp. 259–268 in *Dynamic behavior of materials, I* (Uncasville, CT, 2011), edited by T. Proulx, Springer, New York, 2011.

[Shuck and Advani 1972]  L. Z. Shuck and S. H. Advani, "Rheological response of human brain tissue in shear", *J. Basic Eng. (ASME)* **94**:4 (1972), 905–911.

[Treloar 1975]  L. R. G. Treloar, *The physics of rubber elasticity*, 3rd ed., Clarendon Press, Oxford, 1975.

[Trexler et al. 2011]  M. M. Trexler, A. M. Lennon, A. C. Wickwire, T. P. Harrigan, Q. T. Luong, J. L. Graham, A. J. Maisano, J. C. Roberts, and A. C. Merkle, "Verification and implementation of a modified split Hopkinson pressure bar technique for characterizing biological tissue and soft biosimulant materials under dynamic shear loading", *J. Mech. Behav. Biomed. Mater.* **4**:8 (2011), 1920–1928.

[Truesdell and Noll 1965]  C. Truesdell and W. Noll, *The non-linear field theories of mechanics*, Handbuch der Physik **III/3**, Springer, Berlin, 1965.

[Warren and Forrestal 2010]  T. L. Warren and M. J. Forrestal, "Comments on the effect of radial inertia in the Kolsky bar test for an incompressible material", *Exp. Mech.* **50**:8 (2010), 1253–1255.

[Wylie 1975]  C. R. Wylie, *Advanced engineering mathematics*, 4th ed., McGraw-Hill, New York, 1975.

ADAM SOKOLOW: adam.c.sokolow.civ@mail.mil
*U.S. Army Research Laboratory, Soldier Protection Sciences Branch, Aberdeen Proving Ground, MD 21005, United States*

MIKE SCHEIDLER: michael.j.scheidler2.ctr@mail.mil
*U.S. Army Research Laboratory, Soldier Protection Sciences Branch, Aberdeen Proving Ground, MD 21005, United States*

msp

# JOURNAL OF MECHANICS OF MATERIALS AND STRUCTURES

msp.org/jomms

Founded by Charles R. Steele and Marie-Louise Steele
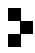
Cover photo: Wikimedia Commons